Title
Molecular hallmarks of heterochronic parabiosis at single-cell resolution

Journal
Nature, 603(7900)

ISSN
0028-0836

Authors
Pálovics, Róbert
Keller, Andreas
Schaum, Nicholas
et al.

Publication Date
2022-03-10

DOI
10.1038/s41586-022-04461-2

Peer reviewed

Article

Molecular hallmarks of heterochronic parabiosis at single-cell resolution

https://doi.org/10.1038/s41586-022-04461-2

Received: 23 October 2020

Accepted: 25 January 2022

Published online: 2 March 2022

Check for updates

Róbert Pálovics[1,43], Andreas Keller[1,2,43]✉, Nicholas Schaum[1,43], Weilun Tan[3,43], Tobias Fehlmann[2], Michael Borja[3], Fabian Kern[2], Liana Bonanno[1], Kruti Calcuttawala[1], James Webber[3], Aaron McGeever[3], The Tabula Muris Consortium*, Jian Luo[4], Angela Oliveira Pisco[3], Jim Karkanias[3], Norma F. Neff[3], Spyros Darmanis[3]✉, Stephen R. Quake[3,5]✉ & Tony Wyss-Coray[1,6,7]✉

The ability to slow or reverse biological ageing would have major implications for mitigating disease risk and maintaining vitality[1]. Although an increasing number of interventions show promise for rejuvenation[2], their effectiveness on disparate cell types across the body and the molecular pathways susceptible to rejuvenation remain largely unexplored. Here we performed single-cell RNA sequencing on 20 organs to reveal cell-type-specific responses to young and aged blood in heterochronic parabiosis. Adipose mesenchymal stromal cells, haematopoietic stem cells and hepatocytes are among those cell types that are especially responsive. On the pathway level, young blood invokes new gene sets in addition to reversing established ageing patterns, with the global rescue of genes encoding electron transport chain subunits pinpointing a prominent role of mitochondrial function in parabiosis-mediated rejuvenation. We observed an almost universal loss of gene expression with age that is largely mimicked by parabiosis: aged blood reduces global gene expression, and young blood restores it in select cell types. Together, these data lay the groundwork for a systemic understanding of the interplay between blood-borne factors and cellular integrity.

Recent transcriptomic studies of major organs and cell types across the lifespan of the mouse (*Tabula Muris Senis*) uncovered both global and tissue/cell-type-specific ageing signatures throughout the body[3–5] providing a first glimpse at how ageing differentially impacts interconnected organs. However, how, or whether, the growing number of rejuvenation paradigms affect these global ageing pathways at a cellular level remains unknown. Heterochronic parabiosis (in which a young and an aged mouse share a common circulation) and systemic infusions of young blood are methods of rejuvenation with broad beneficial effects including on cognition, muscle strength and bone repair in mice[6]; young blood also reversed the DNA methylation age in several organs in rats. Several circulatory proteins have been determined to mediate at least some of the observed effects[1,7–10], but the consequences of parabiosis on distinct organs and cells are incompletely understood.

Here we attempt to address this question by performing Smart-seq2-based single-cell RNA sequencing (scRNA-seq) of C57BL6/JN male mice following 5 weeks of heterochronic parabiosis, when mice had reached 4 and 19 months of age (equivalent to humans aged around 25 and 65 years). Targeted cell populations were captured via flow cytometry into microtitre plates from 20 organs—bladder, brain, brown adipose tissue (interscapular depot), diaphragm, gonadal adipose tissue (GAT; inguinal depot), heart, kidney, large intestine, limb muscle, liver, lung, marrow, mesenteric adipose tissue (MAT), pancreas, skin (epidermis), spleen, subcutaneous adipose tissue (posterior depot), thymus, tongue and trachea—as detailed for each tissue and cell type (Fig. 1a, b, Extended Data Figs. 1, 2, Supplementary Tables 1–3, Supplementary Fig. 1). By integrating single-cell ageing data from the simultaneously collected *Tabula Muris Senis* (Extended Data Fig. 1a), we were able to match cell type annotations per tissue and compare parabiosis-mediated rejuvenation (REJ) and accelerated ageing (ACC) to normal ageing (AGE). Although mice from this parabiosis experiment and *Tabula Muris Senis* originate from the same cohort and were mapped to the same reference with the same parameters, the frozen cells were processed at different times. We therefore performed batch correction to account for technical artefacts (Extended Data Fig. 1j, k). Raw data are available from the Gene Expression Omnibus and a public Amazon Web Service (AWS) S3 bucket, gene–cell counts and metadata are available on Figshare, and the entire annotated dataset is available and accessible online via an interactive browser (see 'Data availability').

Cell-type-specific responses

To determine which cell types are susceptible to ACC or REJ during parabiosis (Fig. 1a), we analysed differential gene expression (DGE) in

[1]Department of Neurology and Neurological Sciences, Stanford University School of Medicine, Stanford, CA, USA. [2]Clinical Bioinformatics, Saarland University, Saarbrücken, Germany. [3]Chan Zuckerberg Biohub, San Francisco, CA, USA. [4]Veterans Administration Palo Alto Healthcare System, Palo Alto, CA, USA. [5]Department of Bioengineering, Stanford University, Stanford, CA, USA. [6]Paul F. Glenn Center for the Biology of Aging, Stanford University School of Medicine, Stanford, CA, USA. [7]Wu Tsai Neurosciences Institute, Stanford University School of Medicine, Stanford, CA, USA. [43]These authors contributed equally: Róbert Pálovics, Andreas Keller, Nicholas Schaum, Weilun Tan. *A list of authors and their affiliations appears at the end of the paper. ✉e-mail: ackeller@stanford.edu; spyros.darmanis@czbiohub.org; steve@quake-lab.org; twc@stanford.edu

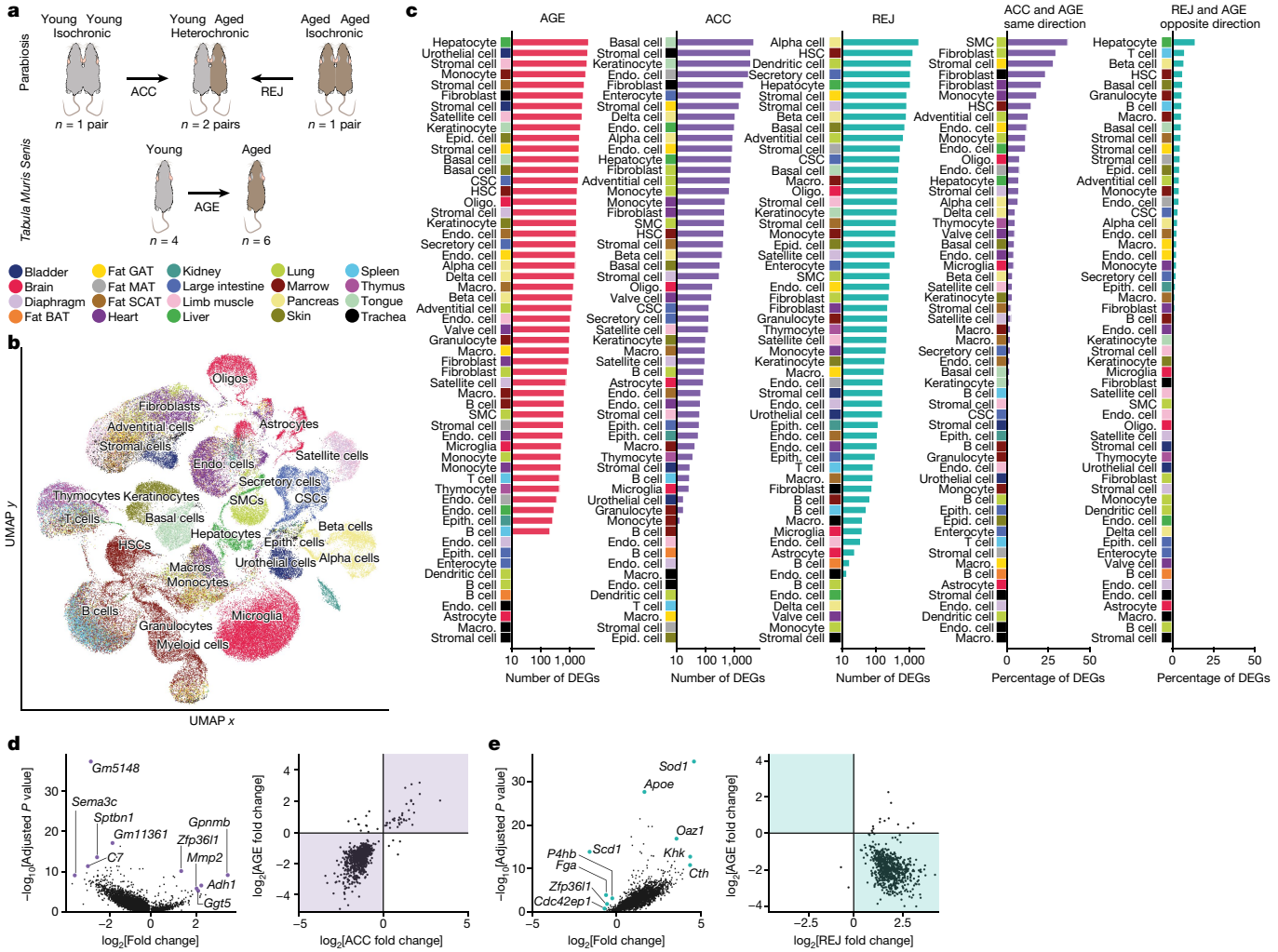

Fig. 1 | Cell-type-specific DGE. a, Experimental outline. Single-cell transcriptomic data were collected from the indicated mice and tissues (Methods). **b**, Uniform manifold approximation and projection visualization of the entire dataset (n = 69,727 cells of parabiosis, n = 52,553 cells of TMS). Cells are coloured by tissue origin (Methods 'Data extraction' and 'Global UMAP visualization'). **c**, Cell types ranked by the percentage/number of DEGs (Wilcoxon–Mann–Whitney test with two-sided, adjusted $P < 0.05$, effect size > 0.6; Methods 'DGE' and 'Analysis of the overlap of DEG sets'). **d**, **e**, DGE results of ACC in fat GAT stromal cells (**d**) and REJ in liver hepatocytes (**e**). Volcano plots (left) show top DEGs. Comparisons of $\log_2$-transformed fold changes (right) show changes with parabiosis (ACC/REJ) on the x axis and with AGE on the y axis. Areas in which ACC and AGE change in the same direction as well as areas in which REJ and AGE change in the opposite direction are highlighted. BAT, brown adipose tissue; CSC, crypt stem cell; endo., endothelial; epid., epidermal; epith., epithelial; macro., macrophage; oligo., oligodendrocyte; SCAT, subcutaneous adipose tissue; SMC, smooth muscle cell.

49 cell types for ACC (isochronic young versus heterochronic young) and 51 cell types for REJ (isochronic aged versus heterochronic aged) from a total of 20 tissues and 122,280 cells. We detect differentially expressed genes (DEGs; adjusted P value < 0.05, effect size > 0.6) in nearly all cell types ranging from tens to thousands of genes (Fig. 1c, Supplementary Fig. 2 and Supplementary Tables 4, 5) with ageing exerting the strongest phenotype in terms of both the number of DEGs and their magnitude of change (Extended Data Fig. 3a–d). Aged blood more closely recapitulates the effects of normal ageing than young blood does reversing it, although generally, parabiosis induces many genes not affected by ageing across most cell types (Fig. 1c). The number of DEGs was not significantly affected by differences in cell number (Extended Data Fig. 3e, f) or biological replicate number (Extended Data Fig. 4a), and differences between groups in percentage mitochondrial genes, ribosomal genes and External RNA Controls Consortium (ERCCs) spike-in controls are not evident (Extended Data Figs. 1f–i, 2e–h). Permuting the experimental groups within each cell type resulted in no DEGs (adjusted $P < 0.05$; effect size > 0.1). Finally, downsampling to 50 cells per biological group revealed stable DEG rankings (Extended Data Fig. 4b), as does iteratively increasing the stringency of the adjusted P value and the area under the curve (Extended Data Fig. 4c), and sequencing saturation analysis uncovered no biases between experiments or conditions (Extended Data Fig. 1l).

At a cell type level, hepatocytes not only show the most DEGs with normal ageing and a strong response to aged blood (Fig. 1c) but also exhibit an equally prominent increase in gene expression (Fig. 1e) and the largest reversal of age-related gene expression changes of any cell type (Fig. 1c, e, Supplementary Table 5) on exposure to young blood. The high perfusion rate of the liver may explain this exceptional responsiveness of hepatocytes, and befittingly, they were one of the first cell types described to undergo rejuvenation during parabiosis[11]. On the other hand, endothelial cells that are in immediate contact with blood, show discrete, tissue-specific transcriptional susceptibility to young or aged blood and are more affected in MAT and GAT, for example, than in muscle (Fig. 1c). Another cell type,

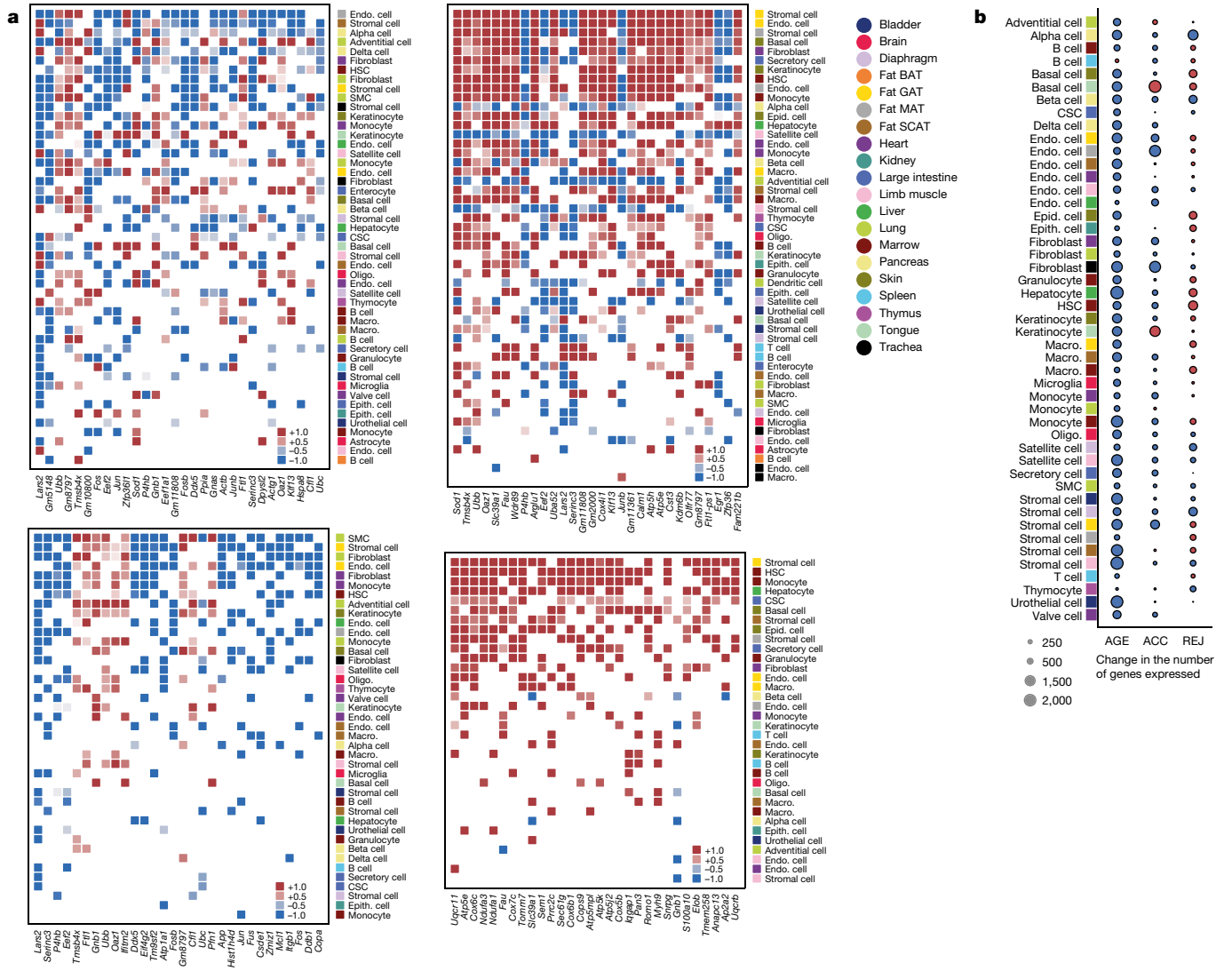

Fig. 2 | Young blood reverses mitochondrial and global gene expression loss. a, Most frequent DEGs shared across several cell types (Wilcoxon–Mann–Whitney test with two-sided adjusted *P* value < 0.05, effect size > 0.6) and their $\log_2$-transformed fold changes for ACC (top left) and REJ (top right). DEGs shared with AGE are indicated at the bottom: DEGs changing in the same direction with AGE and ACC (bottom left) and DEGs changing in the opposite direction with AGE and REJ (bottom right). **b**, Change in the mean number of genes expressed with AGE, ACC and REJ in case of each cell type (Methods 'Analysis of changes in the number of genes expressed').

mesenchymal stromal cells (MSCs), displays large numbers of DEGs in fat tissues, with GAT MSCs undergoing some of the largest gene expression changes of any cell type in response to parabiosis and 28% DEGs in the same direction as AGE (Fig. 1c, d, Supplementary Table 4). These findings may relate to the fact that visceral adipose tissues undergo some of the earliest and most marked transcriptomic changes with age[4], and that the expansion and inflammation of visceral fat is especially detrimental.

Immune cell accumulation across diverse organs is a fundamental feature of ageing[4,12]. We observed that tissue-resident immune cells of both the lymphoid and myeloid lineages are transcriptionally changed by parabiosis, as are their marrow-resident precursors, haematopoietic stem cells (HSCs) (Fig. 1c), perhaps indicating a tight-knit relationship between ageing of the immune system and changes in blood composition. HSCs undergo appreciable age- and parabiosis-related gene expression changes, including enrichment for genes related to mRNA splicing (Extended Data Fig. 5b), consistent with the findings of studies on heterochronic transplantation of marrow or HSCs in mice[13–16]. Moreover, aged HSCs were found to induce circulating cyclophilin A, encoded by *Ppia* (ref. [17]), a gene ranked among the top DEGs across cell types exposed to aged blood (Extended Data Fig. 5a).

We find that aged blood induces many cell-type-specific changes akin to ageing, as can be seen by the large proportion of overlapping DEGs for many cell types (Fig. 1c, Extended Data Fig. 3g–j), whereas rejuvenation is a more concerted process: AGE DEGs rescued by REJ are highly enriched for mitochondrial electron transport chain genes for many cell types (Extended Data Fig. 5c). We note that REJ and AGE also frequently share the same direction of gene expression change possibly pointing to repair and compensatory changes induced by ageing and amplified with parabiosis.

In addition, there are numerous instances in which ACC and REJ have little to no overlap with AGE DEGs (Fig. 1c). The reason for these discordant results is unknown, but it could be that ageing of these cells is influenced more by other factors, masking subtler effects caused by an altered systemic circulation. Overall, these data indicate that nearly all cell types are amenable to reformation via changes to blood composition, even those not directly exposed to blood. Furthermore, we find that ageing of certain cell types—for example, HSCs that give rise to circulating and tissue-resident immune cells—is heavily influenced by the systemic milieu.

Gene-specific responses

One way to assess the effects of parabiosis is to study the top genes in young mice exposed to aged blood that mirror normal ageing, and genes changing with ageing that are reversed by young blood (Fig. 2a, Extended Data Fig. 5a, Supplementary Tables 4, 5). Most conspicuously, across a range of cell types and tissues, young blood reverses the loss of expression in normal ageing of genes encoding electron transport chain subunits such as *Cox6c*, *Cox7c*, *Ndufa1*, *Ndufa3*, *Atp5k* and *Uqcr11*, (Fig. 2a, Extended Data Fig. 5d). Oxidative phosphorylation and the electron transport chain are the top enriched pathways (Extended Data Fig. 5c), with REJ reversing the expression loss of AGE in genes encoding each of the five complexes (Extended Data Fig. 6a). In fact, the top downregulated DEG across all cell types in ACC is that encoding leucyl-tRNA synthetase (*Lars2*), which functions in the translation of mitochondrial encoded genes, and several cell types upregulate *Lars2* in REJ (Fig. 2a). Notably, RNA-mediated interference of *lrs-2* in *Caenorhabditis elegans* was shown to greatly extend lifespan[18]. These single-cell ageing data are consistent with independent bulk organ RNA-seq data across the lifespan and of liver and adipose tissue from an independent cohort, but reveal cell-type-specific phenotypes missed previously (Extended Data Fig. 6b, c), and they support a key role for mitochondrial dysfunction in ageing[1,4].

Modulation of mitochondrial gene expression is but one part of a more global response to differentially aged blood: not only is gene expression loss with age evident in nearly every cell type[19], but this is mimicked by ACC and reversed in select cell types by REJ (Fig. 2b, Extended Data Fig. 7a–f, Supplementary Tables 6–8). These findings support a fundamental role for transcriptional regulation itself in ageing and rejuvenation.

Structured responses

To investigate biological responses during parabiosis in an unbiased way, we identified gene expression pathways in response to ageing and parabiosis for each cell type. Whereas ACC produced responses mostly consistent with, but weaker than, AGE, REJ activated pathways related to cellular respiration very strongly, suggesting enhanced metabolic activity in heterochronic aged parabionts (Fig. 3a, b). Notably, ATP-synthesis-coupled electron transport is the second highest enriched pathway in ACC as well, indicating that mitochondrial function in young cells may also be influenced by external factors (Extended Data Fig. 8a, b). Microglia and HSCs display the most similar overall transcriptional responses to AGE and ACC (Fig. 3c). The presence of mitochondrial electron transport pathways common to these two groups is notable, as such genes commonly arise and overlap between AGE and REJ (Extended Data Fig. 8c, Supplementary Fig. 3). Although aged blood may contribute to age-related decline in some cell populations, young blood can induce mitochondrial genes in cell types in which age-related decline is not especially strong, such as pancreatic beta cells (Extended Data Fig. 8d), supporting the notion that young blood may indeed broadly enhance mitochondrial function.

There are also cell types for which REJ is highly correlated with AGE, exemplified by the stem cell and stem-cell-like populations of satellite cells and MSCs from the diaphragm ($\rho = 0.50$ and 0.48). Notably, the same cell type, present in different organs, often shows highly divergent responses to AGE, ACC and REJ, suggesting a more prominent role of the cellular environment over circulating factors.

Coordinated cellular responses

To assess overarching effects of ageing, we computed the pairwise cosine similarity between each cell type based on their AGE DEG sets. In other words, high similarity will be assigned to two cell types that express similar sets of AGE DEGs. We then first visualize the results

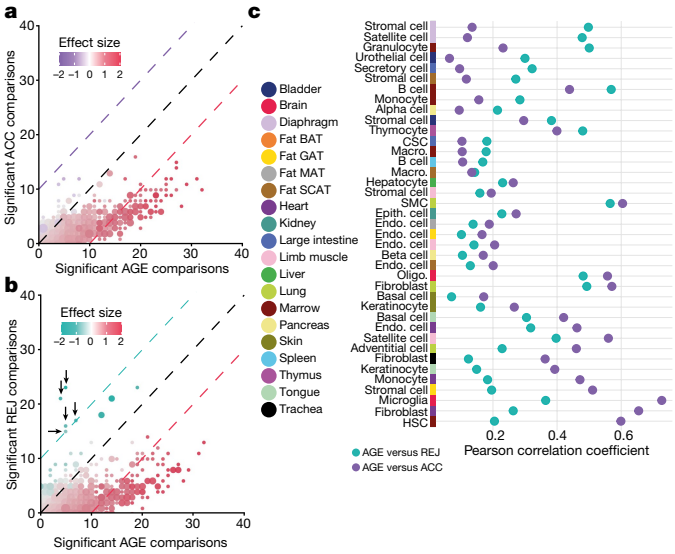

Fig. 3 | Structured responses to parabiosis. a, Scatter plot showing the number of cell types for which pathways are significantly affected in ACC (*y* axis) and AGE (*x* axis). Pathways affected in the same number of comparisons on the *x* axis and *y* axis are grouped together (dot sizes show the size of the groups; Methods 'Pathway analysis'). **b**, As in **a**, comparing significantly affected pathways in REJ and AGE. Mitochondria-related pathways in REJ are highlighted by arrows. **c**, Pearson correlation coefficient for each tissue and cell type comparing pathway profiles between indicated groups.

by plotting the corresponding histogram of similarity scores for all pairwise comparisons (Fig. 4a). After repeating this analysis for ACC and REJ, it is evident that although the highest similarities are observed for AGE, the transcriptomic signatures of REJ show considerable conservation between cell types. Such commonalities are absent in ACC, consistent with divergent pathways arising for top ACC DEGs (Extended Data Fig. 8b). To determine which groups of cell types are responsible for the AGE similarity signature, we plotted the closest connection for each cell type (Fig. 4, Extended Data Fig. 9a–c). Notably, AGE instigates coordinated transcriptomic changes with high similarity within some tissues, particularly pancreas and skin, yet clearly distinct signatures between tissues overall, indicating that local pro-ageing factors or programmes may govern ageing of these tissues. We discovered that cell types such as endothelial cells, MSCs and immune cells share transcriptional programmes of ageing across vastly different and distant tissues, possibly reflecting cell-intrinsic transcriptional programmes of ageing. Indeed, for MSCs across four adipose tissues and two skeletal muscle types, the loss of collagen gene expression forms a core network (Extended Data Fig. 9d, f). It is particularly intriguing that collagen, the main component of the extracellular matrix and produced largely by fibroblasts and stromal cells, has core functions not only in scarring and fibrosis but also in tissue regeneration and maintenance in general. Age-related loss, or indeed gain, of collagen content in different tissues is known to impair homeostatic function, as is extensive collagen crosslinking[20]. In the context of immune cells, it has been speculated that infiltration of these cells may lead to 'spreading' of ageing in invaded tissues through secreted factors[4,21]. Future studies may explore the basis of cellular 'hubs' that are transcriptionally related to many cell types—for example, monocytes of marrow, endothelial cells of subcutaneous adipose tissue—whereas other cell types are less connected.

A similar analysis of parabiosis shows that an aged circulation mimics, in part, the tissue- and cell-type-specific transcriptional similarities, but they are overall less pronounced, and many disappear (Fig. 4). Of note, although skin and marrow maintain solid tissue-wide cellular transcriptomes following exposure to young blood—albeit different

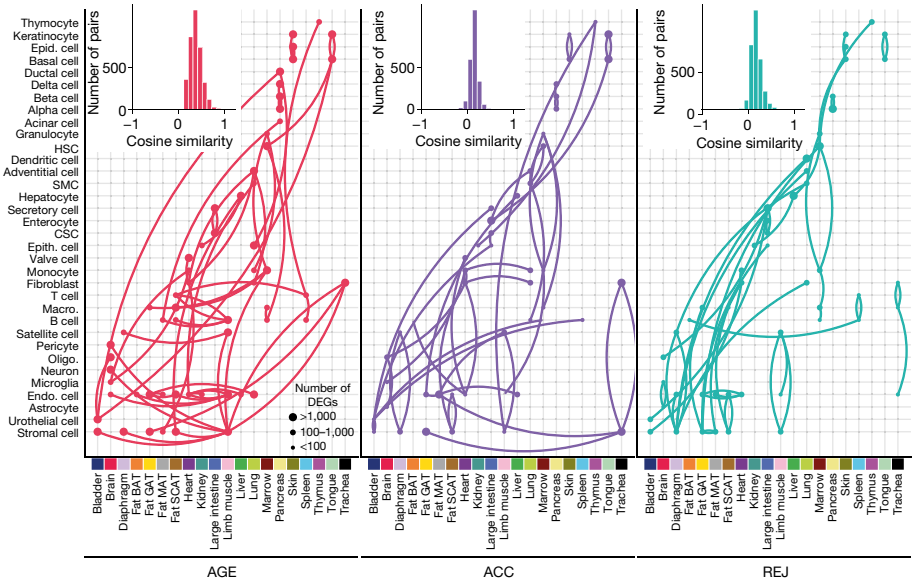

Fig. 4 | Coordinated, organism-wide cellular responses to ageing and parabiosis. Histograms of pairwise cosine similarities that are calculated between each cell type based on the cell-type-specific DGE signatures of AGE, ACC and REJ (Methods 'Ageing and rejuvenation similarity analysis'). Each cell type is connected to its most similar cell type. Cell types of the same tissue are listed vertically, and similar cell types with different tissue of origin are listed horizontally.

from those observed with ageing—many new transcriptional similarities emerge across cell types and tissues. Most notably, REJ triggers similar transcriptional signatures across highly divergent cell types. For example, the mitochondrial electron transport gene node emerges once again as a core rejuvenation network, and is especially strong between MSCs (GAT and MAT), hepatocytes, basal and epidermal cells from skin, and HSCs and macrophages from marrow (Extended Data Fig. 9e, g).

Discussion

Our dataset provides a systematic look into the transcriptomic effects of heterochronic parabiosis at single-cell resolution across the entire organism. Continuous exposure to differentially aged blood alters the transcriptomic landscape across cell types, and we discovered that particular cell types—namely MSCs, HSCs and hepatocytes—are especially susceptible to gene expression changes. Whereas the effects of aged blood tend to accelerate normal ageing changes, young blood both reverses age-related profiles and initiates new pathways. Although the reversal of ageing through young blood may be easier to grasp, it will be equally interesting to explore the molecular and functional as well as therapeutic implications of those distinct pathways. Systemic rejuvenation of genes encoding components of the electron transport chain is especially notable, as is the reversal of global gene expression loss with age. Together, these findings reveal the molecular details of how ageing and parabiosis trigger highly complex global responses across the organism, some of which are tissue specific and some cell type specific, probably reflecting a sophisticated combination of cellular, local and systemic transcriptional cues. These newly discovered transcriptional programmes shared between cell types in response to the three chronogenic environments provide potential avenues for therapeutic interventions, although it remains possible that cell types not included in the study respond differently. Finally, heterochronic parabiosis represents only one rejuvenation paradigm, and organism-wide analysis of other interventions, such as was recently conducted for caloric restriction in rats[12], may help uncover complementary treatments able to comprehensively target ageing hallmarks throughout the body.

Online content

Any methods, additional references, Nature Research reporting summaries, source data, extended data, supplementary information, acknowledgements, peer review information; details of author contributions and competing interests; and statements of data and code availability are available at https://doi.org/10.1038/s41586-022-04461-2.

1. López-Otín, C., Blasco, M. A., Partridge, L., Serrano, M. & Kroemer, G. The hallmarks of aging. *Cell* **153**, 1194–1217 (2013).
2. Mahmoudi, S., Xu, L. & Brunet, A. Turning back time with emerging rejuvenation strategies. *Nat. Cell Biol.* **21**, 32–43 (2019).
3. Schaum, N. et al. Single-cell transcriptomics of 20 mouse organs creates a *Tabula Muris*. *Nature* **562**, 367–372 (2018).
4. Schaum, N. et al. Ageing hallmarks exhibit organ-specific temporal signatures. *Nature* **583**, 596–602 (2020).
5. Almanzar, N. et al. A single-cell transcriptomic atlas characterizes ageing tissues in the mouse. *Nature* **583**, 590–595 (2020).
6. Castellano, J. M., Kirby, E. D. & Wyss-Coray, T. Blood-borne revitalization of the aged brain. *JAMA Neurol.* **72**, 1191–1194 (2015).
7. Villeda, S. A. et al. The ageing systemic milieu negatively regulates neurogenesis and cognitive function. *Nature* **477**, 90–96 (2011).
8. Katsimpardi, L. et al. Vascular and neurogenic rejuvenation of the aging mouse brain by young systemic factors. *Science* **344**, 630–634 (2014).
9. Smith, L. K. et al. β2-microglobulin is a systemic pro-aging factor that impairs cognitive function and neurogenesis. *Nat. Med.* **21**, 932–937 (2015).
10. Khrimian, L. et al. Gpr158 mediates osteocalcin's regulation of cognition. *J. Exp. Med.* **214**, 2859–2873 (2017).
11. Conboy, I. M. et al. Rejuvenation of aged progenitor cells by exposure to a young systemic environment. *Nature* **433**, 760–764 (2005).
12. Ma, S. et al. Caloric restriction reprograms the single-cell transcriptional landscape of *Rattus norvegicus* aging. *Cell* **180**, 984–1001 (2020).
13. Das, M. M. et al. Young bone marrow transplantation preserves learning and memory in old mice. *Commun. Biol.* **2**, 73 (2019).
14. Baht, G. S. et al. Exposure to a youthful circulation rejuvenates bone repair through modulation of β-catenin. *Nat. Commun.* **6**, 7131 (2015).
15. Kovina, M. V., Zuev, V. A., Kagarlitskiy, G. O. & Khodarovich, Y. M. Effect on lifespan of high yield non-myeloablating transplantation of bone marrow from young to old mice. *Front. Genet.* https://doi.org/10.3389/fgene.2013.00144 (2013).
16. Wang, C.-H. et al. Bone marrow rejuvenation accelerates re-endothelialization and attenuates intimal hyperplasia after vascular injury in aging mice. *Circ. J.* **77**, 3045–3053 (2013).
17. Smith, L. K. et al. The aged hematopoietic system promotes hippocampal-dependent cognitive decline. *Aging Cell* **19**, e13192 (2020).
18. Lee, S. S. et al. A systematic RNAi screen identifies a critical role for mitochondria in *C. elegans* longevity. *Nat. Genet.* **33**, 40–48 (2003).

19. Zhang, M. J., Pisco, A. O., Darmanis, S. & Zou, J. Mouse Aging Cell Atlas analysis reveals global and cell type specific aging signatures revision 1. *Elife* **10**, e62293 (2021).
20. Kular, J. K., Basu, S. & Sharma, R. I. The extracellular matrix: structure, composition, age-related differences, tools for analysis and applications for tissue engineering. *J. Tissue Eng.* **5**, https://doi.org/10.1177/2041731414557112 (2014).
21. Pinti, M. et al. Aging of the immune system: focus on inflammation and vaccination. *Eur. J. Immunol.* **46**, 2286–2301 (2016).
22. Villeda, S. A. et al. Young blood reverses age-related impairments in cognitive function and synaptic plasticity in mice. *Nat. Med.* **20**, 659–663 (2014).

The Tabula Muris Consortium

Nicole Almanzar[8], Jane Antony[9], Ankit S. Baghel[9], Isaac Bakerman[9,10,11], Ishita Bansal[9], Ben A. Barres[12], Philip A. Beachy[7,9,13,14,15], Daniela Berdnik[1], Biter Bilen[1], Douglas Brownfield[13], Corey Cain[16], Charles K. F. Chan[17], Michelle B. Chen[5], Michael F. Clarke[9], Stephanie D. Conley[3], Spyros Darmanis[3], Aaron Demers[3], Kubilay Demir[9,14], Antoine de Morree[1,18], Tessa Divita[3], Haley du Bois[4], Hamid Ebadi[3], F. Hernán Espinoza[13], Matt Fish[9,14,15], Qiang Gan[1], Benson M. George[9], Astrid Gillich[13], Rafael Gòmez-Sjöberg[3], Foad Green[3], Geraldine Genetiano[3], Xueying Gu[15], Gunsagar S. Gulati[9], Oliver Hahn[1], Michael Seamus Haney[1], Yan Hang[15], Lincoln Harris[3], Mu He[19], Shayan Hosseinzadeh[3], Albin Huang[1], Kerwyn Casey Huang[3,5,20], Tal Iram[1], Taichi Isobe[9], Feather Ives[3], Robert C. Jones[3], Kevin S. Kao[9], Jim Karkanias[3], Guruswamy Karnam[21], Andreas Keller[1,2,43], Aaron M. Kershner[9], Nathalie Khoury[1], Seung K. Kim[15,22], Bernhard M. Kiss[9,23], William Kong[9], Mark A. Krasnow[13,14], Maya E. Kumar[24,25], Christin S. Kuo[8], Jonathan Lam[15], Davis P. Lee[1], Song E. Lee[1], Benoit Lehallier[1], Olivia Leventhal[4], Guang Li[11,26], Qingyun Li[12], Ling Liu[1], Annie Lo[3], Wan-Jin Lu[9,13], Maria F. Lugo-Fagundo[1], Anoop Manjunath[9], Andrew P. May[3], Ashley Maynard[3], Aaron McGeever[3], Marina McKay[3], M. Windy McNerney[27,28], Bryan Merrill[20], Ross J. Metzger[29,30], Marco Mignardi[5], Dullei Min[8], Ahmad N. Nabhan[13], Norma F. Neff[3], Katharine M. Ng[13], Patricia K. Nguyen[9,10,11], Joseph Noh[9], Roel Nusse[13,14,15], Róbert Pálovics[1,43], Rasika Patkar[21], Weng Chuan Peng[15,31], Lolita Penland[3], Angela Oliveira Pisco[3], Katherine Pollard[32], Robert Puccinelli[3], Zhen Qi[9], Stephen R. Quake[3,5], Thomas A. Rando[1,4,6], Eric J. Rulifson[15], Nicholas Schaum[1,43], Joe M. Segal[21], Shaheen S. Sikandar[9], Rahul Sinha[9,33,34,35], Rene V. Sit[3], Justin Sonnenburg[3,20], Daniel Staehli[1], Krzysztof Szade[9,36], Michelle Tan[3], Weilun Tan[3,43], Cristina Tato[3], Krissie Tellez[15], Laughing Bear Torrez Dulgeroff[9], Kyle J. Travaglini[13], Carolina Tropini[20,37,38,39], Margaret Tsui[21], Lucas Waldburger[3], Bruce M. Wang[21], Linda J. van Weele[9], Kenneth Weinberg[8], Irving L. Weissman[9,33,34,35], Michael N. Wosczyna[1], Sean M. Wu[8,10,11,14], Tony Wyss-Coray[1,6,7], Jinyi Xiang[9], Soso Xue[5], Kevin A. Yamauchi[3], Andrew C. Yang[1,5], Lakshmi P. Yerra[1], Justin Youngyunpipatkul[3], Brian Yu[3], Fabio Zanini[5], Macy E. Zardeneta[1,6], Alexander Zee[3], Chunyu Zhao[3], Fan Zhang[29,30], Hui Zhang[1], Martin Jinye Zhang[40,41], Lu Zhou[12] & James Zou[3,40,42]

[8]Department of Pediatrics, Pulmonary Medicine, Stanford University School of Medicine, Stanford, CA, USA. [9]Institute for Stem Cell Biology and Regenerative Medicine, Stanford University School of Medicine, Stanford, CA, USA. [10]Stanford Cardiovascular Institute, Stanford University School of Medicine, Stanford, CA, USA. [11]Division of Cardiovascular Medicine, Department of Medicine, Stanford University School of Medicine, Stanford, CA, USA. [12]Department of Neurobiology, Stanford University School of Medicine, Stanford, CA, USA. [13]Department of Biochemistry, Stanford University School of Medicine, Stanford, CA, USA. [14]Maternal & Child Health Research Institute, Stanford University School of Medicine, Stanford, CA, USA. [15]Department of Developmental Biology, Stanford University School of Medicine, Stanford, CA, USA. [16]Flow Cytometry Core, Veterans Administration Palo Alto Healthcare System, Palo Alto, CA, USA. [17]Department of Surgery, Division of Plastic and Reconstructive Surgery, Stanford University, Stanford, CA, USA. [18]Department of Biomedicine, Aarhus University, Aarhus, Denmark. [19]Department of Physiology, University of California, San Francisco, CA, USA. [20]Department of Microbiology & Immunology, Stanford University School of Medicine, Stanford, CA, USA. [21]Department of Medicine and Liver Center, University of California San Francisco, San Francisco, CA, USA. [22]Department of Medicine and Stanford Diabetes Research Center, Stanford University, Stanford, CA, USA. [23]Department of Urology, Stanford University School of Medicine, Stanford, CA, USA. [24]Sean N. Parker Center for Asthma and Allergy Research, Stanford University School of Medicine, Stanford, CA, USA. [25]Department of Medicine, Division of Pulmonary and Critical Care, Stanford University School of Medicine, Stanford, CA, USA. [26]Department of Developmental Biology, University of Pittsburgh School of Medicine, Pittsburgh, PA, USA. [27]Mental Illness Research Education and Clinical Center, Veterans Administration Palo Alto Healthcare System, Palo Alto, CA, USA. [28]Department of Psychiatry, Stanford University School of Medicine, Stanford, CA, USA. [29]Vera Moulton Wall Center for Pulmonary and Vascular Disease, Stanford University School of Medicine, Stanford, CA, USA. [30]Department of Pediatrics, Division of Cardiology, Stanford University School of Medicine, Stanford, CA, USA. [31]Princess Máxima Center for Pediatric Oncology, Utrecht, The Netherlands. [32]Department of Epidemiology and Biostatistics, University of California, San Francisco, CA, USA. [33]Department of Pathology, Stanford University School of Medicine, Stanford, CA, USA. [34]Ludwig Center for Cancer Stem Cell Research and Medicine, Stanford University School of Medicine, Stanford, CA, USA. [35]Stanford Cancer Institute, Stanford University School of Medicine, Stanford, CA, USA. [36]Department of Medical Biotechnology, Faculty of Biochemistry, Biophysics and Biotechnology, Jagiellonian University, Krakow, Poland. [37]School of Biomedical Engineering, University of British Columbia, Vancouver, British Columbia, Canada. [38]Department of Microbiology and Immunology, University of British Columbia, Vancouver, British Columbia, Canada. [39]Humans and the Microbiome Program, Canadian Institute for Advanced Research, Toronto, Ontario, Canada. [40]Department of Electrical Engineering, Stanford University, Palo Alto, CA, USA. [41]Department of Epidemiology, Harvard T.H. Chan School of Public Health, Boston, MA, USA. [42]Department of Biomedical Data Science, Stanford University, Palo Alto, CA, USA.

Methods

Experimental procedures

Parabiosis and organ collection. Male 3-month-old and 18-month-old C57BL/6JN mice were shipped from the National Institute on Ageing colony at Charles River (housed at 19–23 °C) to the Veterinary Medical Unit (VMU; housed at 20–24 °C, humidity ranged from 30–70%)) at the VA Palo Alto (VA). At both locations, mice were housed on a 12 h/12 h light/dark cycle and provided with food and water ad libitum. The diet at Charles River was NIH-31, and at the VA VMU it was Teklad 2918. Littermates were not recorded or tracked, and mice were housed at the VA VMU for no longer than 2 weeks before surgery.

Parabiosis via the peritoneal method was accomplished by suturing together the peritoneum of adjacent flanks, forming a continuous peritoneal cavity. To promote coordinated movement, adjacent knee joints and elbow joints were joined with nylon monofilament sutures. Skin was joined with surgical autoclips. All procedures were conducted with aseptic conditions on heating pads, with mice under continuous isoflurane anaesthesia. To prevent infection, limit pain and promote hydration, mice were injected with Baytril (5 μg g^{-1}), buprenorphine and 0.9% (w/v) sodium chloride, as described previously[6,22]. Pairs remained together for 5 weeks before organ collection.

After anaesthetization with 2.5% v/v Avertin at 8:00, mice were weighed and shaved, and blood was drawn via cardiac puncture before transcardial perfusion with 20 ml PBS. MAT was then immediately collected to avoid exposure to the liver and pancreas perfusate, which negatively affects cell sorting. Isolating viable single cells from both the pancreas and the liver of the same mouse was not possible; therefore, only one was collected from each mouse. Whole organs were then dissected in the following order: large intestine, spleen, thymus, trachea, tongue, brain, heart, lung, kidney, GAT, bladder, diaphragm, limb muscle (tibialis anterior), skin (dorsal), subcutaneous adipose tissue (inguinal pad), brown adipose tissue (interscapular pad), aorta and bone marrow (spine and limb bones). Organ collection concluded by 10:00. After single-cell dissociation as described below, cell suspensions were used for FACS of individual cells into 384-well plates. All animal care and procedures were carried out in accordance with institutional guidelines approved by the VA Palo Alto Committee on Animal Research.

Sample size, randomization and blinding. No sample size choice was performed before the study. Blinding was not performed: the authors were aware of all data- and metadata-related variables during the entire course of the study.

Tissue dissociation and sample preparation. All tissues were processed as previously described[5].

Single-cell methods. All protocols used in this study are described in detail elsewhere[3,5]. These include: preparation of lysis plates; FACS sorting; cDNA synthesis using the Smart-seq2 protocol[23,24]; library preparation using an in-house version of Tn5 (refs. [25,26]); library pooling and quality control; and sequencing. For further details, see https://www.protocols.io/view/smartseq2-for-htp-generation-of-facs-sorted-single-2uwgexe.

Computational methods

Data extraction. Sequences from the NovaSeq were demultiplexed using bcl2fastq version 2.20. Reads were aligned with Gencode v.M19 annotations using STAR version 2.5.2b with parameters TK. Gene counts were produced using HTSEQ version 0.6.1p1 with default parameters, except stranded was set to false, and mode was set to intersection-nonempty. We merged these data with scRNA-seq profiles of cells from young (3-month-old males) and aged (combined 18-month-old and 24-month-old males) mice from the *Tabula Muris Senis* Smart-seq2 data[4,5]. All subsequent data processing and analysis is conducted on this merged dataset. Note that we chose to merge the 18- and 24-month-old data from *Tabula Muris Senis* to bolster the low cell counts of 18 month olds alone and improve the robustness of downstream analyses.

Quality control. We applied standard filtering rules following the guideline of Luecken and Theis[27]. We discarded cells with fewer than 500 genes, fewer than total 5,000 reads, more than 30% ERCC control reads, more than 10% mitochondrial reads or more than 10% ribosomal reads. Counts were then cpm scaled and log normalized for downstream analysis. Saturation analysis was performed with the scanpy.pp.downsample_counts function of the Scanpy package. Analysis was implemented in Python (3.8.3) with the Scanpy[28] (1.6.0) package.

Data integration and clustering. We merged the data from *Tabula Muris Senis* and the parabionts and grouped the data on the basis of tissue of origin. The top 5,000 highly variable genes were selected and 20 principal components were calculated within each tissue. The number of principal components was identified with the elbow method. We then used the BBKNN batch correction algorithm[29] to integrate data from *Tabula Muris Senis* and the parabionts. BBKNN calculates a batch-corrected neighbourhood graph from the imputed principal components. We set the individual mouse IDs as batch labels and hence corrected not only for data-specific batch effects, but also for potential mouse-specific batch effects. Given the large number of mice in total, we set to query one neighbour per batch.

We then used the batch-corrected, tissue-specific neighbourhood graphs to run Leiden clustering[30] and to calculate UMAP embeddings[31] within each tissue. To infer the quality of batch correction, we calculated entropy batch mixing on the batch-corrected neighbourhood graphs. Furthermore, we calculated average LISI scores[32] from the UMAP embeddings. To show potential changes within these metrics due to batch correction, we calculated tissue-specific neighbourhood graphs without any batch correction and repeated the subsequent analysis steps on these neighbourhood graphs. Note that for every downstream analysis we used then the batch-corrected tissue-specific results. All analysis steps except for calculating batch entropy mixing and LISI scores were run in Python (3.8.3) by using the Scanpy[28] (1.6.0) package, BBKNN[29] (1.3.6) and umap-learn[31] (0.3.1). The batch entropy mixing calculation was implemented with Numpy (1.18.1), Pandas (1.1.1) and Scikit-learn[33] (0.22.1). LISI scores were calculated with the LISI R package[32].

Cell type annotation. We used the cell type annotations of *Tabula Muris Senis* to annotate cells from the parabionts. As *Tabula Muris Senis* includes some highly specific annotations, first we joined some of these to achieve more robust results. These merging rules can be found in Supplementary Table 1, in which we list for each cell type label from *Tabula Muris Senis* the corresponding label we used. Then, we used the tissue-specific, batch-corrected neighbourhood graphs containing one neighbour per mouse for each cell, and labelled each cell from the parabiosis experiment on the basis of its network neighbourhood with majority voting. We calculated the most frequent cell type among the cell's neighbours from *Tabula Muris Senis* and used this to annotate the cell. Analysis was implemented in Python (3.8.3), with the Numpy (1.18.1), Pandas (1.1.1), Scanpy (1.6.0) and Scikit-learn (0.22.1) packages.

Global UMAP visualization. Once each cell was annotated, solely for visualization purposes we reran the highly variable gene selection, principal component analysis, batch correction and UMAP calculation steps by using the whole, log–cpm-normalized dataset. These results are not used in any of the downstream analyses but are provided to present an overview of the entire dataset.

DGE. We systematically analysed parabiosis signatures across three comparisons (AGE: Y–A, ACC: IY–HY, REJ: IA–HA) within each identified cell type of each tissue with at least 50 cells per control and treatment groups. We conducted single-cell DGE for the three comparisons within each cell type separately. Specifically, we computed standard $\log_2$[fold changes] as well as the non-parametric unpaired Wilcoxon–Mann–Whitney test[34] for each gene. Two-sided *P* values were corrected with the Benjamini–Hochberg procedure[35] (false discover rate = 0.05) per cell type and comparison. Finally, we identified genes differentially expressed with effect size > 0.6 and adjusted *P* value < 0.05. Note that filtering for effect size is especially important because single-cell data often contain large sample sizes with thousands of cells per condition and effect size cutoffs are not sensitive to sample size. We discarded genes used for quality-control filtering (Rb* and Mt-*) from the DGE analysis as these may be biased by the quality-control process. To investigate the effect of downsampling on the DGE analysis, we used the scanpy.pp.subsample method of scanpy and sampled 50 cells per condition. We then repeated all of the steps of DGE on the subsampled data. Analysis was implemented in Python (3.8.3) with the Numpy (1.18.1), Pandas (1.1.1) and Scanpy (1.6.0) packages.

Analysis of the overlap of DEG sets. We investigated the potential overlap of AGE DEGs and parabiosis (ACC and REJ) DEGs. First, within each cell type we calculated the contingency table of upregulated and downregulated genes with AGE and ACC. These 3 × 3 tables (a gene may be upregulated, not changing or downregulated) include the union of all DEGs of AGE and ACC. We considered genes consistent if they changed in the same direction with AGE and ACC and calculated the fraction of these out of the total number of DEGs defined as the union of AGE and ACC DEGs. Similarly, we defined genes changing in the opposite direction with AGE and ACC as inconsistent. We ran chi-square tests to validate the significance of the overlaps and performed Fisher's exact test for post hoc analysis to investigate the significance of consistent and inconsistent overlaps. We conducted a similar analysis between AGE and REJ except for defining genes that changed in the opposite direction with AGE and REJ as consistent and genes that changed in the same direction with AGE and REJ as inconsistent. Analysis was implemented in Python (3.8.3) with Numpy (1.18.1), Pandas (1.1.1) and Scipy (1.5.1).

Analysis of changes in the number of genes expressed. For each cell, the number of genes expressed was calculated as the number of genes with at least one count. Then, we grouped the data by cell type, tissue and condition (Y, A, IY, HY, IA, HA) and calculated the mean number of genes expressed per group. Next, we computed changes in the mean number of genes expressed of each cell type within each cell type across AGE (Y–A), ACC (IY–HY) and REJ (IA–HA). In addition, we asked whether changes across these comparisons are general and hence not cell type specific. We performed regression analyses with linear mixed effects models separately for AGE, ACC and REJ. We sampled 50 cells equally per cell type from both control (AGE: Y, ACC: IY, REJ: IA) and treatment (AGE: A, ACC: HY, REJ: HA) groups. Next we ran a linear mixed effects model in which we set the number of genes expressed as a dependent variable, mouse replicate as a random effect, and finally the cell type, sequencing depth and group (control or treatment) attributes as independent variables. Finally, we investigated the potential effect of transcriptional noise. We grouped the data by condition (Y, A, IY, HY, IA, HA) and cell type and calculated cell–cell variability and overdispersion[36,37]. Analysis was implemented in Python (3.8.3) with Numpy (1.18.1), Pandas (1.1.1) and statsmodels (0.12.0).

Pathway analysis. Gene set enrichment analysis was performed using GeneTrail 3 (ref. [38]) on the basis of the expressed genes and the results were sorted such that the most significantly upregulated genes were at the beginning of the list and the most significantly downregulated ones were at the end, using the Gene Ontology[39] category biological process. *P* values were adjusted for multiple testing using the Benjamini–Hochberg procedure[35]. Pathways that were significantly enriched or depleted were counted as being significantly affected. Results were analysed with the programming language R (4.0.2). To generate the enrichment heatmaps, the 30 most enriched categories of each comparison were extracted. The rows were clustered with Ward's clustering criterion and Euclidean distance. Pathways were determined to be related to mitochondria by ensuring that at least 25% of the genes associated with the corresponding pathway were present in MitoCarta 3.0 (ref. [40]). The heatmaps were plotted with the ComplexHeatmap[41] (2.4.2) R package. The scatter plot comparing the number of significantly affected cell types and tissues by AGE, REJ or ACC pathways was plotted with ggplot2 (ref. [42]; 3.3.2). The effect size was determined by computing the difference between the $\log_{10}$-transformed enrichment *P* values of the corresponding pathway (AGE and parabiosis, ACC or REJ). The effect size of several pathways was defined as the average effect size of all single pathways. For visualization purposes, to control outliers, the effect sizes were clipped between −2.5 and 2.5. To determine the most differently affected pathways per comparison, we filtered similar terms using the GOSemSim R package (2.14.0) according to the Jiang measure with a cutoff at a similarity of 0.7. We computed for every setup comparison the per tissue and cell type similarity of the determined enrichment *P* values on the negative $\log_{10}$-transformed values by using Pearson's correlation coefficient.

Ageing and rejuvenation similarity analysis. We base these analyses on the DGE results. We define similarities between cell types for the three comparisons (AGE, ACC, REJ) separately. First, for a specific comparison we select genes that are differentially expressed with effect size > 0.6, adjusted *P* value < 0.05 per cell type. Next, we take the vectors indicating the $\log_2$[fold changes] across these genes per cell type. We compute the cosine similarities of those vectors and hence calculate pairwise similarities between the cell types. We present the structure of these similarity networks in our results. Analysis was implemented in Python (3.8.3) with the Gseapy (0.10.1), Networkx[43] (2.5.0), Numpy (1.18.1), Pandas (1.1.1), Scanpy (1.6.0), Scikit-learn (0.22.1) and Seaborn (0.11.0) packages.

STRING network analysis. For each set of DEGs of interest, we queried the STRING database[44] for links with >0.9 confidence.

Bulk RNA-seq validation experiments. Tissue samples were collected and processed as previously described[2]. Following library preparation, 180 samples were sequenced on a single lane on a NovaSeq 6000 machine configured for 150-bp paired-end reads. Raw sequencing files were demultiplexed using Illumina bcl2fastq. Unfiltered FASTQ files were then processed using the RNA-seq pipeline (3.0) of the nf-core project[45]. In brief, the pipeline consists of quality-control analysis, adapter trimming, read mapping and filtering using STAR (ref. [46]), post-alignment sorting and filtering, transcription quantification with RSEM (ref. [47]), and further quality-control statistics. As the associated reference, the mouse genome GRCm38 along with the GENCODE vM19 genomic feature release was used. Raw transcript and gene abundances per sample were loaded with the tximport package[48] (1.18.0) in the statistical programming language R (4.0.5). Samples with fewer than 5 million reads per sample were removed from further analysis. Imported counts of valid samples were then processed with DESeq2 (ref. [49]; 1.30.1) for read count normalization based on sample sequencing depth and effective gene lengths and differential expression analysis at standard parameters but alpha level set to 0.05. Resulting log-scaled fold changes were shrunk using the standard normal approach. To map Ensembl gene IDs to gene names, we used the corresponding mapping as specified in the GENCODE vM19 annotation file. For reading and writing of data files and tables, we used the R packages data.table (1.14.0), openxlsx (4.2.3) and readr (1.4.0).

Reporting summary

Further information on research design is available in the Nature Research Reporting Summary linked to this paper.

Code availability

Code used for downstream analyses of the raw count matrices is available at GitHub:https://github.com/rpalovics/parabiosis/releases/tag/0.1.0 (https://doi.org/10.5281/zenodo.5762659).

Data availability

The dataset can be explored interactively at https://ccb-web.cs.uni-saarland.de/parabiosis/. Gene counts and metadata are available on Figshare: https://figshare.com/projects/Molecular_hallmarks_of_heterochronic_parabiosis_at_single_cell_resolution/127628. Raw sequencing data are available in the Gene Expression Omnibus under accession code GSE132042 and via the following public AWS S3 bucket: https://registry.opendata.aws/tabula-muris-senis/. The versions of the noted databases used are available at the following URLs: STRING database, https://version-11-0.string-db.org/; MitoCarta 3.0, https://www.broadinstitute.org/files/shared/metabolism/mitocarta/mouse.mitocarta3.0.html; GENCODE vM19, https://www.gencodegenes.org/mouse/release_M19.html.

23. Picelli, S. et al. Full-length RNA-seq from single cells using Smart-seq2. *Nat. Protoc.* **9**, 171–181 (2014).
24. Darmanis, S. et al. A survey of human brain transcriptome diversity at the single cell level. *Proc. Natl Acad. Sci. USA* **112**, 7285–7290 (2015).
25. Picelli, S. et al. Tn5 transposase and tagmentation procedures for massively scaled sequencing projects. *Genome Res.* **24**, 2033–2040 (2014).
26. Hennig, B. P. et al. Large-scale low-cost NGS library preparation using a robust Tn5 purification and tagmentation protocol. *G3 (Bethesda)* **8**, 79–89 (2018).
27. Luecken, M. D. & Theis, F. J. Current best practices in single-cell RNA-seq analysis: a tutorial. *Mol. Syst. Biol.* **15**, e8746 (2019).
28. Wolf, F. A., Angerer, P. & Theis, F. J. SCANPY: large-scale single-cell gene expression data analysis. *Genome Biol.* **19**, 15 (2018).
29. Polański, K. et al. BBKNN: fast batch alignment of single cell transcriptomes. *Bioinformatics* **36**, 964–965 (2020).
30. Traag, V. A., Waltman, L. & Van Eck, N. J. From Louvain to Leiden: guaranteeing well-connected communities. *Sci. Rep.* **9**, 5233 (2019).
31. McInnes, L., Healy, J. & Melville, J. UMAP: Uniform Manifold Approximation and Projection for Dimension Reduction. Preprint at https://arxiv.org/abs/1802.03426 (2018) .
32. Korsunsky, I. et al. Fast, sensitive and accurate integration of single-cell data with Harmony. *Nat. Methods* **16**, 1289–1296 (2019).
33. Pedregosa, F. et al. Scikit-learn: machine Learning in Python. *J. Machine Learn. Res.* **12**, 2825–2830 (2011).
34. Mann, H. B. & Whitney, D. R. On a test of whether one of two random variables is stochastically larger than the other. *Ann. Math. Stat.* **18**, 50–60 (1947).
35. Benjamini, Y. & Hochberg, Y. Controlling the false discovery rate: a practical and powerful approach to multiple testing. *J. R. Stat. Soc. B* **57**, 289–300 (1995).
36. Enge, M. et al. Single-cell analysis of human pancreas reveals transcriptional signatures of aging and somatic mutation patterns. *Cell* **171**, 321–330 (2017).
37. Kimmel, J. C. et al. Murine single-cell RNA-seq reveals cell-identity- and tissue-specific trajectories of aging. *Genome Res.* **29**, 2088–2103 (2019).
38. Gerstner, N. et al. GeneTrail 3: advanced high-throughput enrichment analysis. *Nucleic Acids Res.* **48**, W515–W520 (2020).
39. Carbon, S. et al. The Gene Ontology Resource: 20 years and still GOing strong. *Nucleic Acids Res.* **47**, D330–D338 (2019).
40. Rath, S. et al. MitoCarta3.0: an updated mitochondrial proteome now with sub-organelle localization and pathway annotations. *Nucleic Acids Res.* **49**, D1541–D1547 (2021).
41. Gu, Z., Eils, R. & Schlesner, M. Complex heatmaps reveal patterns and correlations in multidimensional genomic data. *Bioinformatics* **32**, 2847–2849 (2016).
42. Wickham, H. ggplot2. *Wiley Interdiscip. Rev. Comput. Stat.* **3**, 180–185 (2011).
43. Hagberg, A., Swart, P. & Schult, D. Exploring Network Structure, Dynamics, and Function Using Networkx (Los Alamos National Laboratory, 2008); https://www.osti.gov/servlets/purl/960616.
44. Szklarczyk, D. et al. STRING v11: protein–protein association networks with increased coverage, supporting functional discovery in genome-wide experimental datasets. *Nucleic Acids Res.* **47**, D607–D613 (2019).
45. Ewels, P. A. et al. The nf-core framework for community-curated bioinformatics pipelines. *Nat. Biotechnol.* **38**, 276–278 (2020).
46. Dobin, A. et al. STAR: ultrafast universal RNA-seq aligner. *Bioinformatics* **29**, 15–21 (2013).
47. Li, B. & Dewey, C. N. RSEM: accurate transcript quantification from RNA-Seq data with or without a reference genome. *BMC Bioinform.* **12**, 323 (2011).
48. Soneson, C., Love, M. I. & Robinson, M. D. Differential analyses for RNA-seq: transcript-level estimates improve gene-level inferences [version 1; peer review: 2 approved]. *F1000Research* **4**, 1521 (2015).
49. Love, M. I., Huber, W. & Anders, S. Moderated estimation of fold change and dispersion for RNA-seq data with DESeq2. *Genome Biol.* **15**, 550 (2014).
50. Chen, E. Y. et al. Enrichr: interactive and collaborative HTML5 gene list enrichment analysis tool. *BMC Bioinform.* **14**, 128 (2013).

Acknowledgements We thank the members of the laboratory of T.W.-C. and the Chan Zuckerberg Biohub for feedback and support. Financial support for library preparation, sequencing and AWS time was provided by the Chan Zuckerberg Biohub. Further financial support was provided by the Department of Veterans Affairs (BX004599 to T.W.-C.), the National Institute on Aging (R01-AG045034, AG064928, AG072255, and DP1-AG053015 to T.W.-C.), the NOMIS Foundation (T.W.-C.), The Glenn Foundation for Medical Research (T.W.-C.), Nan Fung Life Sciences (T.W.-C.), and the Wu Tsai Neurosciences Institute and Bertarelli Foundation (T.W.-C.). This work was supported by the National Institute of Aging and the National Institutes of Health under award number P30AG059307.

Author contributions R.P., A.K., N.S. and W.T. contributed equally. N.S., S.R.Q. and T.W.-C. conceptualized the study. R.P., A.K., N.S., T.F. and T.W.-C. conceptualized the analysis. R.P., A.K., T.F. and F.K. conducted the analysis. N.S., L.B. and J.L. performed parabiosis surgeries. N.S. and K.C. collected and processed bulk organ samples for RNA-seq. The Tabula Muris Consortium processed organs and captured cells for scRNA-seq. W.T. and M.B. conducted cDNA and library preparation. R.P. created the web browser. W.T. and M.B. performed sequencing and library quality control. W.T., M.B., A.O.P., J.W. and A.M. processed raw sequencing data. R.P., A.K., N.S., S.R.Q. and T.W.-C. wrote and edited the manuscript. T.W.-C., S.R.Q., S.D., N.F.N., J.K. and A.O.P supervised the work.

Competing interests The authors declare no competing interests.

Additional information

Supplementary information The online version contains supplementary material available at https://doi.org/10.1038/s41586-022-04461-2.

Correspondence and requests for materials should be addressed to Andreas Keller, Spyros Darmanis, Stephen R. Quake or Tony Wyss-Coray.

Peer review information *Nature* thanks Johan Auwerx, Yousin Suh, Fan Zhang and the other, anonymous, reviewer(s) for their contribution to the peer review of this work.

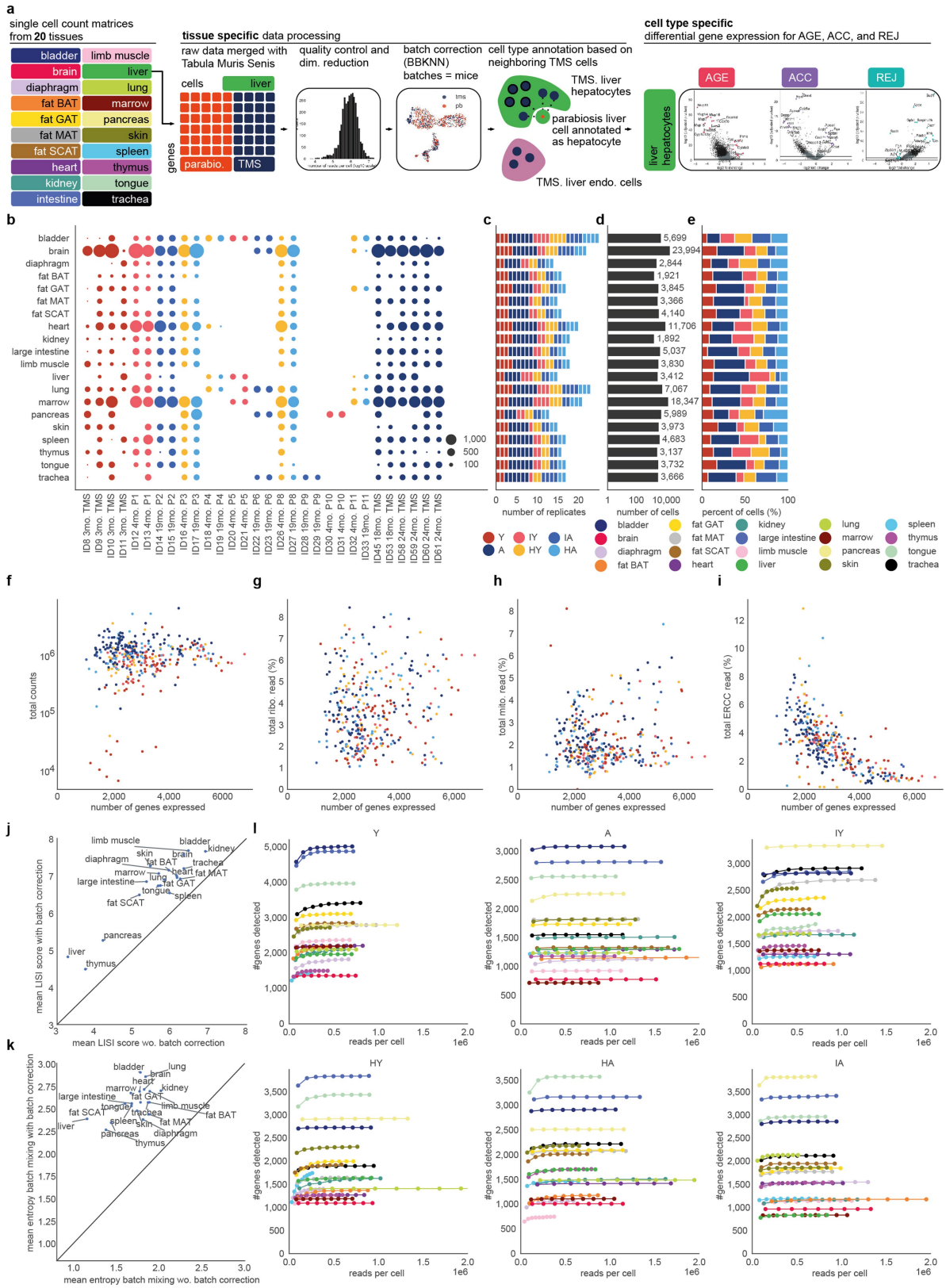

Extended Data Fig. 1 | See next page for caption.

Extended Data Fig. 1 | Outline of data analyses and tissue specific data overview. a, Outline of computational analyses. Single-cell count data are processed per tissue, see Methods 'Quality control'-'Cell type annotation'. Differential gene expression is then conducted per cell type and comparison (AGE, ACC, REJ) within each tissue, see Methods 'Differential gene expression'. All of the next panels present data after quality control. **b**, Number of cells per tissue and replicate. Replicates are colored by their condition. **c**, Number of replicates per tissue. Replicates are colored by their condition. **d**, Total number of cells per tissue. **e**, Fraction of cells within each condition per tissue. **f-i**, For each experimental condition within each tissue: total read counts (**f**), the percent of reads mapped to ribosomal genes (**g**), mitochondrial genes (**h**), and ERCC spike-ins (**i**) plotted against the mean number of genes expressed. **j**, Average LISI scores of mouse replicates calculated over the batch corrected tissue specific UMAP embeddings plotted against the mean LISI scores of tissue specific UMAP embeddings calculated from neighborhood graphs without batch correction. **k**, Mean entropy batch mixing of mouse replicates calculated over the tissue specific batch-corrected neighborhood graph plotted against the mean entropy batch mixing calculated from neighborhood graphs without batch correction. **l**, Result of saturation analyses shown per condition (Y, A, IY, HY, IA, HA). Downsampling was carried out per condition within each tissue separately. Results indicate the number of detected genes as the function of the downsampled total counts.

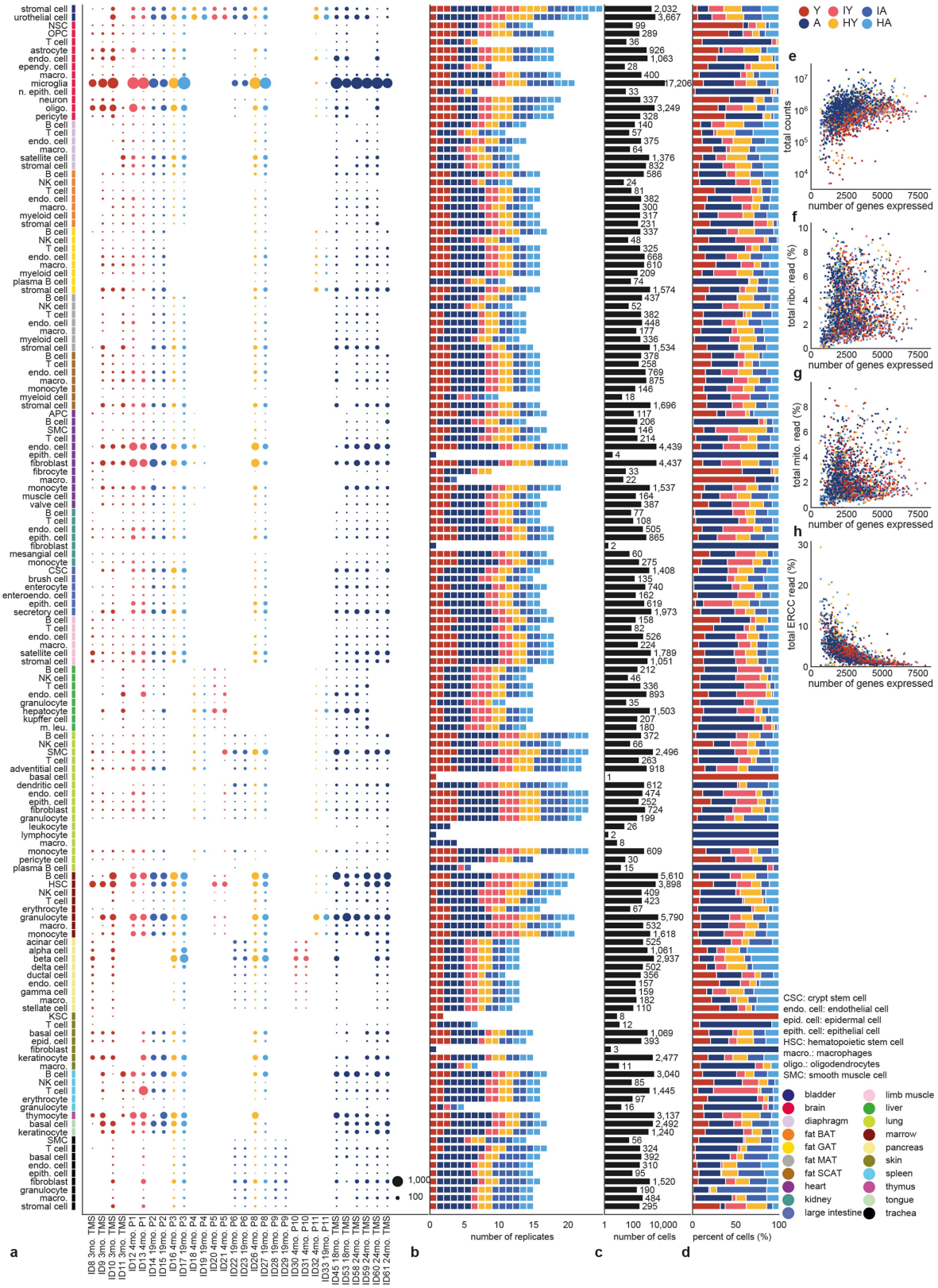

Extended Data Fig. 2 | Cell type specific data overview. All panels present data after quality control. **a**, Number of cells per cell type and replicate. Replicates are colored by their condition. **b**, Number of replicates per cell type. Replicates are colored by their condition. **c**, Total number of cells per cell type. **d**, Fraction of cells within each condition per cell type. **e**-**h**, For each experimental condition within each cell type, total read counts (**e**), the percent of reads mapped to ribosomal genes (**f**), mitochondrial genes (**g**), and ERCC spike-ins (**h**) plotted against the mean number of genes expressed.

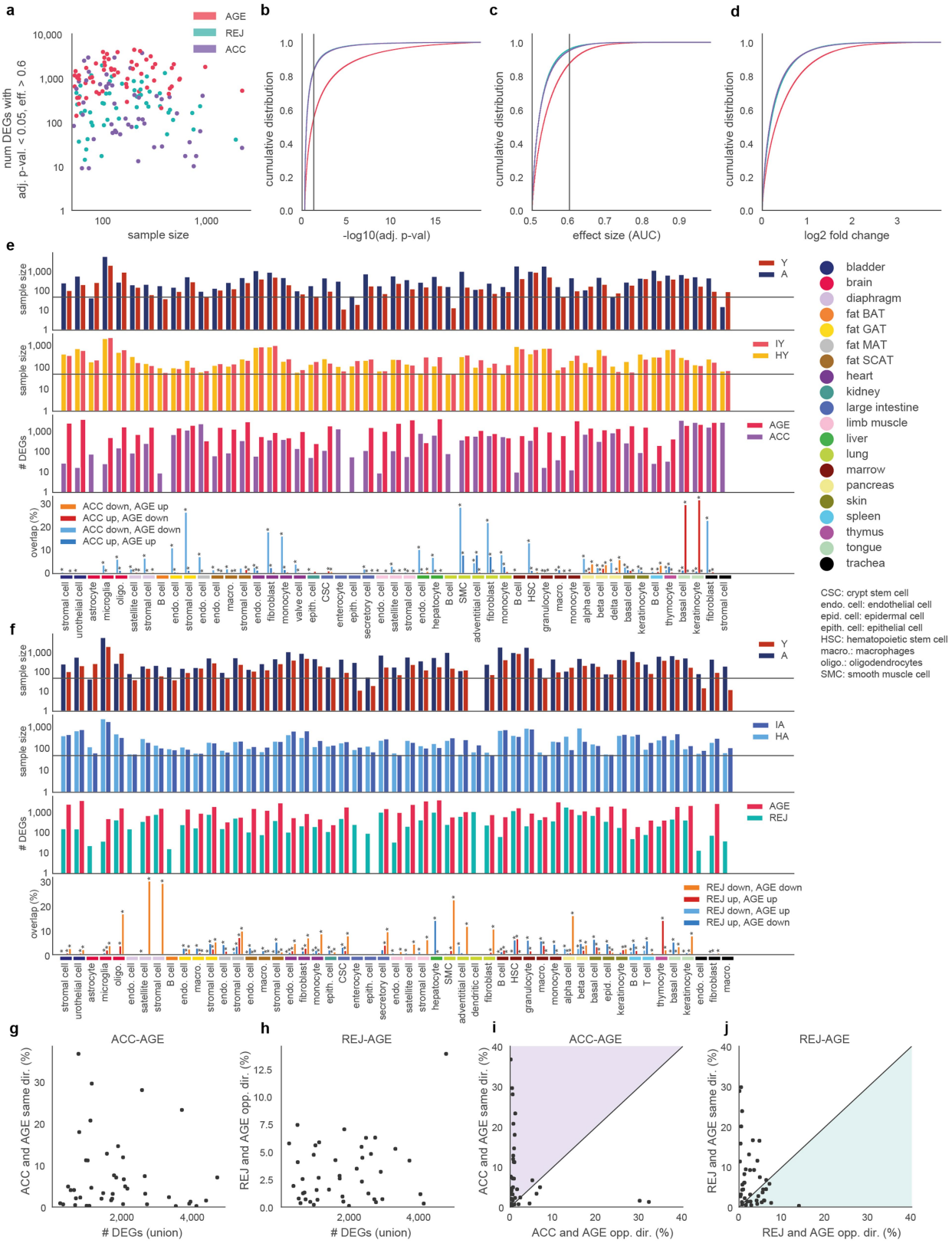

Extended Data Fig. 3 | See next page for caption.

Extended Data Fig. 3 | Validation of differential gene expression analysis. **a**, Number of DEGs plotted against the total number of cells within the control and treatment groups. Each dot represents a DGE comparison of a cell type. **b-d**, Cumulative distributions of the calculated effect size (**b**), -log10(adj. p-value) (**c**) and log2 fold change values (**d**). Distributions are shown separately for ACC, REJ and AGE DGE. Vertical lines indicate the cutoffs applied throughout the study. **e**, Summary of ACC DGE results. Each cell type that has at least 50 cells in IY and HY is studied in the context of ACC and hence shown. From top to bottom: control and treatment sample sizes indicated separately for AGE and ACC, the number of genes differentially expressed in AGE and ACC, overlaps between AGE and ACC. Overlaps are normalized by the number of DEGs in the union of ACC and AGE DEGs. **f**, Summary of REJ DGE results. Each cell type that has at least 50 cells in IA and HA is studied in the context of REJ and hence shown. From top to bottom: control and treatment sample sizes indicated separately for AGE and REJ, the number of genes differentially expressed in AGE and REJ, overlaps between AGE and REJ. Overlaps are normalized by the number of DEGs in the union of REJ and AGE DEGs. **g**, Percent of DEGs that change in the same direction with AGE and ACC are plotted against the total number of DEGs within AGE and ACC for each comparison. Percentages are based on the union of DEGs as defined in (**e**) **h**, Percent of DEGs that change in the opposite direction with AGE and REJ are plotted against the total number of DEGs within AGE and REJ for each comparison. Percentages are based on the union of DEGs as defined in (**f**). **i**, Fraction of DEGs changing in the same direction with AGE and ACC plotted against the fraction of DEGs changing in the opposite direction with AGE and ACC. Each dot represents a cell type of the study. Colored area indicates where more DEGs change in the same direction than in the opposite direction. **j**, Fraction of DEGs changing in the same direction with AGE and REJ plotted against the fraction of DEGs changing in the opposite direction with AGE and REJ. Each dot represents a cell type of the study. Colored area indicates where more DEGs change in the opposite direction than in the same direction.

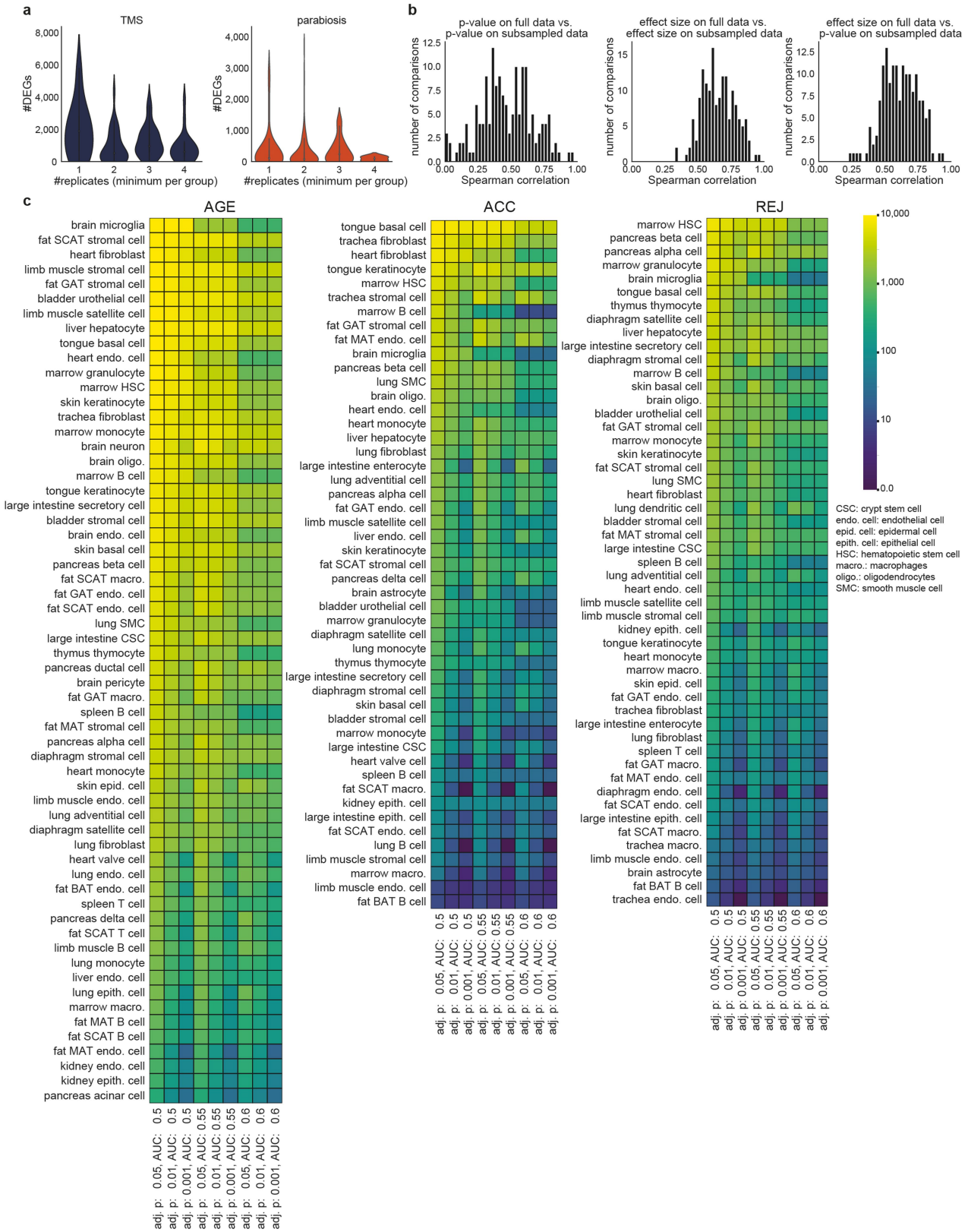

Extended Data Fig. 4 | Validation of differential gene expression analysis. **a**, Violin plots showing the number of differentially expressed genes as the function of the number of replicates per comparison. The number of replicates are defined as the minimum number of replicates within the control and treatment groups. Results are shown separately for TMS (left) and parabiosis (right). **b**, Comparison of differential gene expression results with and without subsampling in case of each cell type specific comparison. Spearman correlation values indicate (dis)similarities between: p-values derived from the original and subsampled data (left), effect sizes calculated from the original and subsampled data (middle), and effect sizes calculated on the original data and p-values derived from the subsampled datasets. **c**, Number of DEGs identified at different p-value and effect size cutoffs per comparison in AGE (left), ACC (middle), and REJ (right).

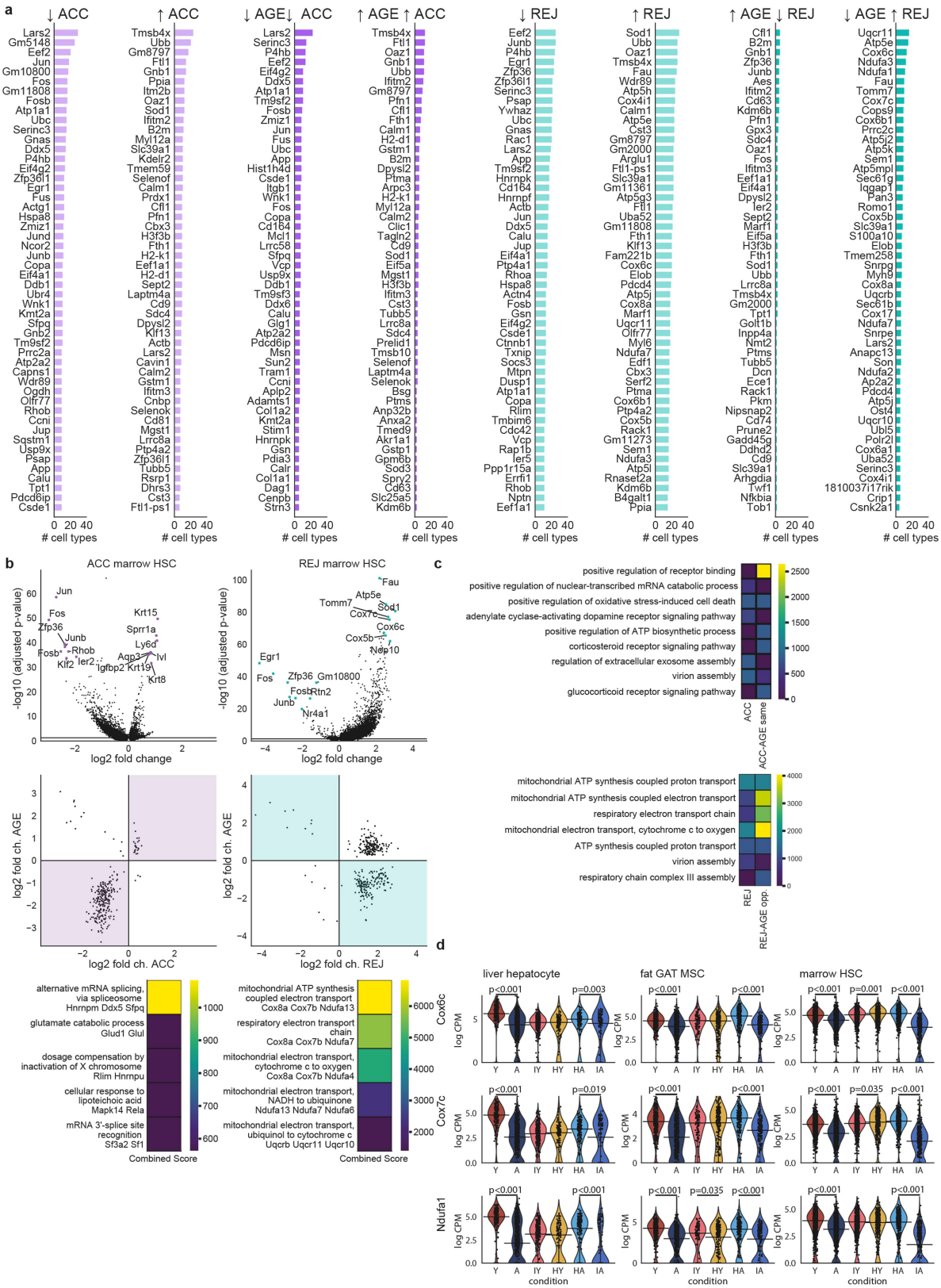

Extended Data Fig. 5 | See next page for caption.

Extended Data Fig. 5 | Differential gene expression results. a, Top list of the 50 most frequent DEGs identified for ACC and REJ. Results are shown separately for up and downregulation. Columns with darker bars indicate top lists where only changes consistent with AGE are shown. These include genes changing in the same direction with ACC and AGE, as well as genes changing in the opposite direction with REJ and AGE. **b**, DGE results for marrow HSCs for ACC (left) and for REJ (right). from top to bottom: volcano plots (top) show top DEGs. Comparisons of log2-fold changes (middle) show changes with parabiosis on the x-axis and with normal ageing on the y-axis. DEGs with adj. p-value < 0.05, eff. size > 0.6 are shown. Areas where ACC and AGE change in the same direction as well as where REJ and AGE change in the opposite direction are highlighted. Top pathways (GO Biological Process) with highest 'Combined scores' defined as in Enrichr[50] are shown at the bottom. **c**, Most enriched pathways (GO Biological Process) among the 100 most frequent DEGs shared across multiple cell types. Results shown for ACC and ACC-AGE same direction (top), and REJ and REJ-AGE opposite direction (bottom). Combined scores are defined as in Enrichr[50]. **d**, Gene expression violin plots for liver hepatocytes, GAT MSCs and marrow HSCs of select genes encoding proteins of the electron transport chain. Significance values show the adj. p-values of the Wilcoxon–Mann–Whitney test (two-sided) based differential gene expression, see Methods: 'Differential gene expression'.

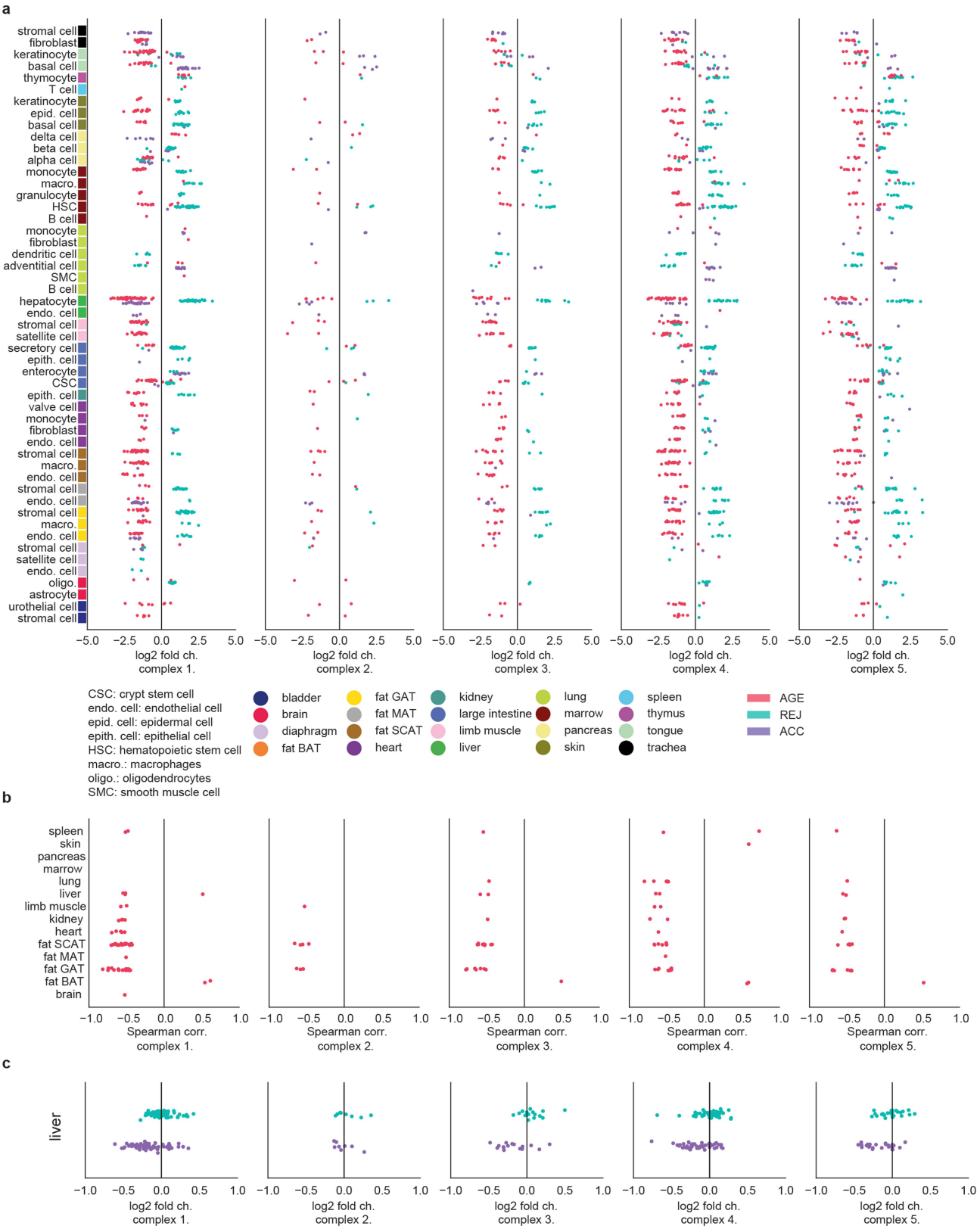

Extended Data Fig. 6 | Analyses of genes associated with the 5 OXPHOS complexes. a, Log2-fold changes with AGE, ACC and REJ of genes associated with the 5 OXPHOS complexes. Changes with adj. p-val.<0.05 and eff. size>0.6 are shown. Each column corresponds to one complex and the three separate colors distinguish between AGE, ACC and REJ. **b**, Spearman correlation of gene expression values with age in case of genes associated with the 5 OXPHOS complexes in the Tabula Muris Senis bulk dataset. Data has been analyzed as in[2]. Correlation values with adj. p-value < 0.05 are shown. **c**, Log2-fold changes with ACC and REJ of genes associated with the 5 OXPHOS complexes in the bulk parabiosis dataset.

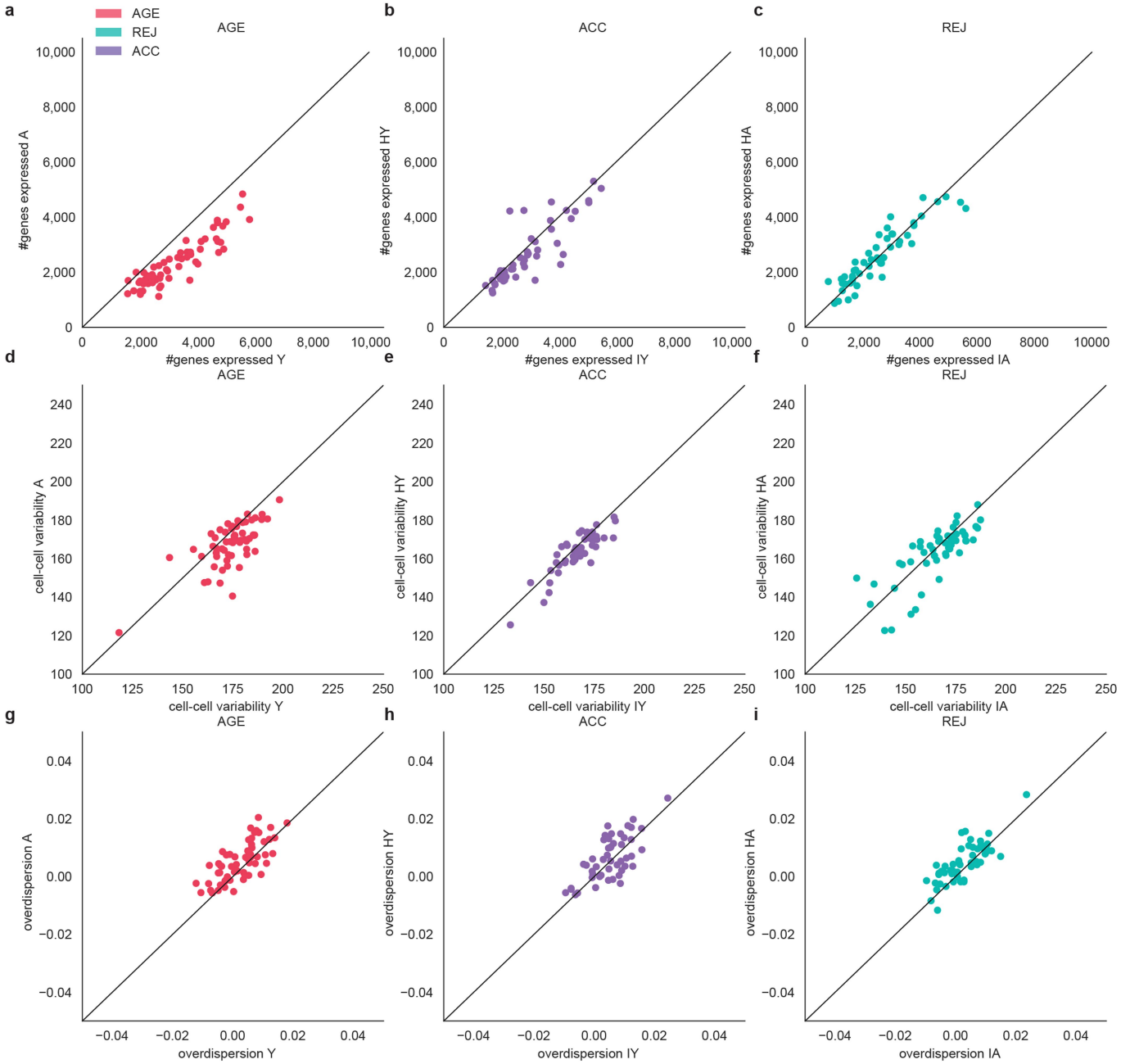

Extended Data Fig. 7 | Analysis of transcriptional noise. a–**c**, Mean number of genes expressed within each cell type, x and y axes indicate Y and A (**a**), IY and HY (**b**) and IA and HA (**c**), each dot represents a cell type. **d**–**f**, Cell-cell variability within each cell type in Y and A (**d**), IY and HY (**e**) and IA and HA (**f**), each dot represents a cell type. **g**–**i**, Overdispersion within each cell type in Y and A (**g**), IY and HY (**h**) and IA and HA (**i**), each dot represents a cell type.

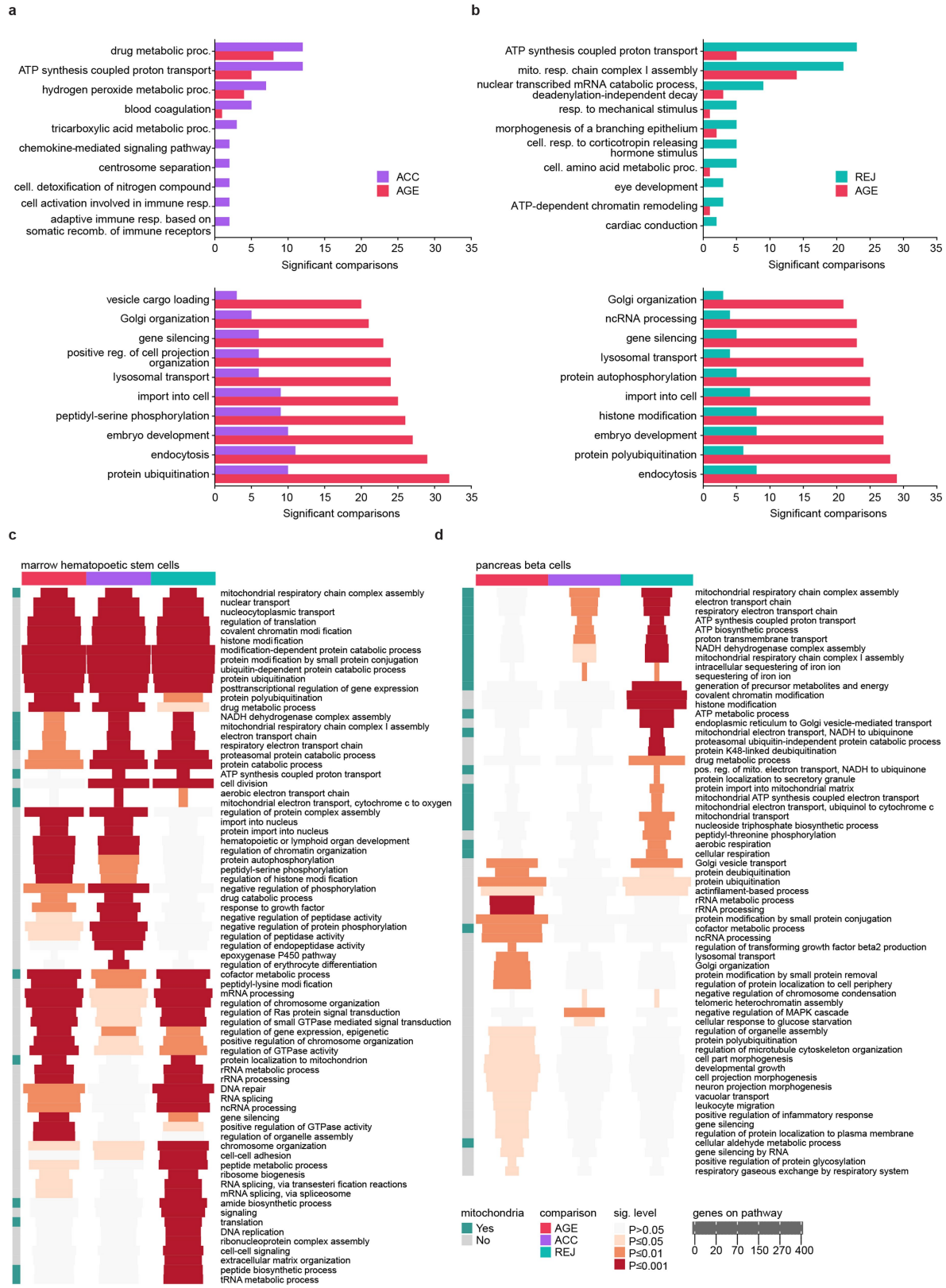

Extended Data Fig. 8 | Pathway analysis. a, Top 10 most differently affected pathways over all ACC tissues and cell types (top, largest difference at the top) and top 10 most differently affected pathways over all AGE (bottom, largest difference at the bottom) tissues and cell types. **b**, Same as for **a**, comparing REJ and AGE pathways. **c**, Heatmap showing the top 30 most strongly affected pathways in AGE, ACC and REJ in hematopoietic stem cells (HSCs) of the marrow. Pathways related to mitochondria are highlighted in green on the left. Each entry of the heatmap shows the significance level and the number of genes associated with the pathway. **d**, Same as for **c**, showing the top 30 most strongly affected pathways for beta cells of the pancreas.

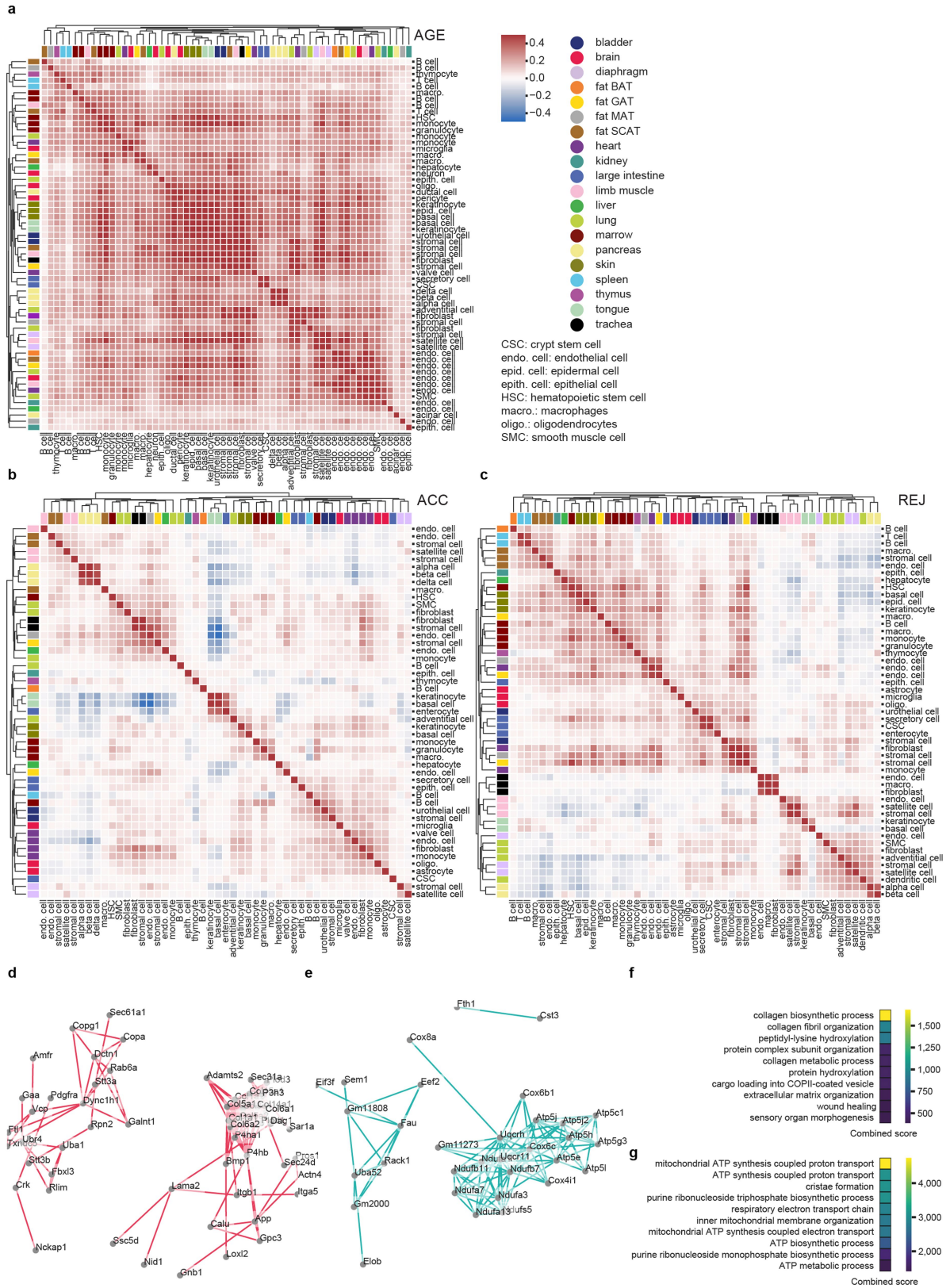

Extended Data Fig. 9 | Ageing and rejuvenation similarity analysis. a–**c**, AGE (**a**), ACC (**b**), and REJ (**c**) DGE based cosine similarity matrices of the cell types studied, see Methods section 'Ageing and rejuvenation similarity analysis'. All matrices are clustered with complete link hierarchical clustering. **d**, Force-directed network visualization of the STRING links between DEGs common to MSCs from GAT, MAT, SCAT, bladder, limb muscle, and diaphragm. **e**, Force-directed network visualization of the STRING links between DEGs common to MSCs (GAT and MAT), hepatocytes, basal and epidermal cells (skin), and HSCs and macrophages (marrow). All links with >0.9 STRING confidence score (scale from 0-1) are queried and shown. **f, g** Most enriched pathways (GO Biological Process) among the nodes of the networks shown in (**d, e**), combined scores are defined as in Enrichr[50].